RESOURCE GEOLOGY

doi: 10.1111/j.1751-3928.2011.00178.x *Resource Geology* Vol. 62, No. 1: 19–41

**Thematic Article**

# Mineralogy and Mineral Chemistry of the Cretaceous Duolong Gold-Rich Porphyry Copper Deposit in the Bangongco Arc, Northern Tibet

Jinxiang Li, Guangming Li, Kezhang Qin, Bo Xiao, Lei Chen and Junxing Zhao

*Key Laboratory of Mineral Resources, Institute of Geology and Geophysics, Chinese Academy of Sciences, Beijing, China*

**Abstract**

The Early Cretaceous Duolong gold-rich porphyry copper deposit is a newly discovered deposit with proven 5.38 Mt Cu resources of 0.72% Cu and 41 t gold of 0.23 g $t^{-1}$ in northern Tibet. Granodiorite porphyry and quartz diorite porphyrite are the main ore-bearing porphyries. A wide range of hydrothermal alteration associated with these porphyries is divided into potassic, argillic and propylitic zones from the ore-bearing porphyry center outward and upward. In the hydrothermal alteration zones, secondary albite (91.5–99.7% Ab) occurs along the rim of plagioclase phenocryst and fissures. Secondary K-feldspar (75.1–96.9% Or) replaces plagioclase phenocryst and matrix or occurs in veinlets. Biotite occurs mainly as matrix and veinlet in addition to phenocryst in the potassic zone. The biotite are Mg-rich and formed under a highly oxidized condition at temperatures ranging from 400°C to 430°C. All the biotites are absent in F, and have high Cl content (0.19–0.26%), with log ($X_{Cl}/X_{OH}$) values of –2.74 to –2.88 and IV (Cl) values of –3.48 to –3.35, suggesting a significant role of chloride complexes ($CuCl_2^-$ and $AuCl_2^-$) in transporting and precipitating copper and gold. Chlorites are present in all alteration zones and correspond mainly to pycnochlorite. They have similar Fe/(Fe+Mg), Mn/(Mn+Mg) ratios, and a formation temperature range of 280–360°C. However, the formation temperature of chlorite in the quartz-gypsum-carbonate-chlorite vein is between 190°C and 220°C, indicating that it may have resulted from a later stage of hydrothermal activity. $Fe^{3+}/Fe^{2+}$ ratios of chlorites have negative correlation with $Al^{IV}$, suggesting oxygen fugacity of fluids increases with decreasing temperature. Apatite mineral inclusions in the biotite phenocrysts show high $SO_3$ content (0.44–0.82%) and high Cl content (1–1.37%), indicating the host magma had a high oxidation state and was enriched in S and Cl. The highest Cl content of apatite in the propylitic zone may have resulted from pressure decrease, and the lowest Cl content of apatite in the argillic zone may have been caused by a low Cl content in the fluids. The low concentration of $SO_3$ content in the hydrothermal apatite compared to the magmatic one may have resulted from the decrease of oxygen fugacity and S content in the hydrothermal fluid, which are caused by the abundant precipitation of magnetite.

**Keywords:** Bangongco arc, Duolong, gold-rich porphyry copper deposit, mineral chemistry, mineralogy.

## 1. Introduction

The Duolong gold-rich porphyry copper deposit was recently discovered by the No.5 Geological Team of the Bureau of Tibetan Geology and Exploration in 2000, together with a super-large prospect (proven Cu resources of 5.38 Mt, 0.72% Cu; 41 t gold, 0.23 g $t^{-1}$ Au) in the Bangongco arc in northern Tibet. At this deposit,

Received 28 June 2010. Accepted for publication 26 October 2011.
Corresponding authors: G. LI and J. LI, Key Laboratory of Mineral Resources, Institute of Geology and Geophysics, Chinese Academy of Sciences, Beijing 100029, China. Emails: lgm@mail.iggcas.ac.cn, ljx@mail.iggcas.ac.cn

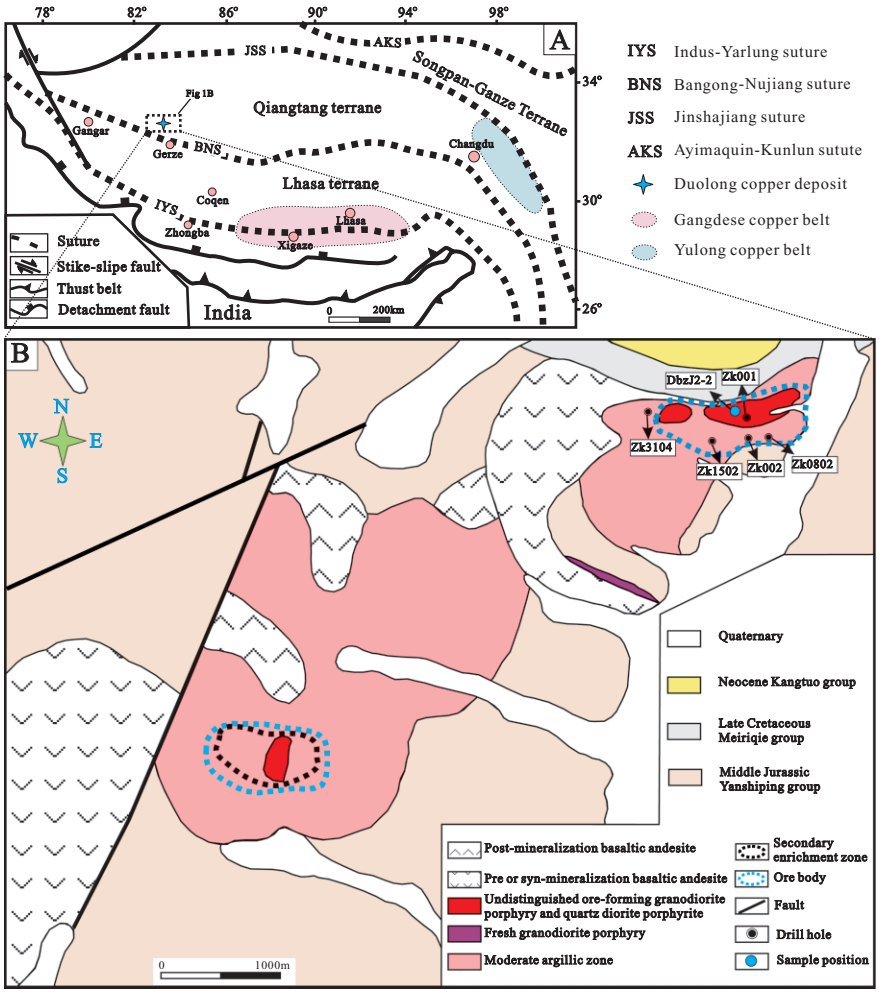


**Fig. 1** Sketch tectonic and location map (a) (after Hou *et al*., 2004) and the generalized geologic map (b) of the Duolong gold-rich porphyry copper deposit (Li *et al*., 2008).

abundant magnetite is associated with Cu-Au mineralization. This deposit is related to relatively mafic quartz diorite porphyrite and granodiorite porphyry in a magmatic arc setting (Li *et al*., 2007, 2012; Li *et al*., 2008). Due to the discovery of the Duolong deposit, the Bangongco Mesozoic arc now becomes the third porphyry copper belt with potential epithermal Au mineralization (Qin *et al*., 2006) (Fig. 1a) following the Yulong (Hou *et al*., 2003, 2007) and Gangdese porphyry copper belts (Hou *et al*., 2004, 2009; Qin *et al*., 2005, 2008) in the Qinghai-Tibet plateau. Although the Duolong deposit has been studied in terms of fluid inclusions characteristics (Li *et al*., 2007), geochronology and geochemistry (Li *et al*., 2008), no investigation focusing on the hydrothermal minerals has been conducted. In this study, we describe the chemical composition of the secondary K-feldspar, albite, chlorite, apatite, biotite, magnetite, rutile and sulfide in the Duolong deposit by systematic electron-probe microscopic analyses, and discuss their geochemical and petrological significance and the evolution of magmatic-hydrothermal fluid.

## 2. Geological settings and ore deposit geology

The Duolong gold-rich porphyry copper deposit is located roughly 100 km northwest of Gereze county at the north of the Bangongco–Nujiang suture zone (Fig. 1a). This deposit formed in a Cretaceous continental arc setting (Qin *et al*., 2006; Li *et al*., 2008). The ore-bearing granodiorite porphyry yields a zircon

SHRIMP U-Pb age of 121.6 ± 1.9 Ma (Li *et al*., 2008), and secondary K-feldspar yields a $^{40}Ar$-$^{39}Ar$ plateau age of 115.2 ± 1.1 Ma (Li *et al*., 2011a). These ages indicate that this deposit formed in the Early Cretaceous and resulted from the subduction of the Neo-Tethys Ocean. The strata consist mainly of the Middle Jurassic Yanshiping Group, the Late Cretaceous Meiriqie Group, the Early Tertiary Kangtuo Group and the Quaternary (Fig. 1b). The Middle Jurassic Yanshiping Group is a clastic-interbedded volcanic sequence of littoral facies, which strikes east-west and dips 50–80°WNW. It is composed of feldspar quartz sandstone, siltstone-interbedded siliceous rock, basalt and dacite. The Late Cretaceous Meiriqie Group contains basaltic andesite, dacite, volcanic-clastic rocks, phenocryst-rich andesite and andesite. The Early Tertiary Kangtuo Group is composed of the brown-red clay and sandy gravel.

### 2.1 Magmatic activity

The Early Cretaceous hypabyssal volcanic rocks mainly contain granodiorite porphyry and quartz diorite porphyrite, which intruded into the Middle Jurassic Yanshiping Group. These intrusive rocks occur as stock and dike, and host mineralization (Fig. 1b). They are exposed to the surface in the northeastern and southeastern portions of the ore district. The granodiorite porphyry shows a spindly shape (width of 200 m and length of 1000 m) and the quartz diorite porphyrite elliptical shape (width of 200 m and length of 300 m). The volcanic rocks (Fig. 1b) are divided into pre-mineralization and post-mineralization basaltic andesite and andesite. The geochemical characteristics of the porphyries and volcanic rocks show that they have the same characteristics as arc magmatism (Li *et al*., 2008): calc-alkaline series, depletion of high field strength elements (such as Nb, Ta, Zr and Hf), and enrichment in large ion lithophile elements (such as Rb and Ba) in basaltic volcanic rocks ($SiO_2$ 49–53%), andesite ($SiO_2$ 58%) and granodiorite porphyry ($SiO_2$ 65–68%).

### 2.2 Hydrothermal alteration

Hydrothermal alteration, comprising mainly of albitization, biotitization, K-feldspathization, sericitization, silicification, epidotization, chloritization, illitization and kaolinization, develop over an area more than 18 $km^2$ around the intrusive rocks. The wall rock alteration zonation is divided into potassic zone, argillic zone and propylitic zone from the ore-bearing porphyry center outward and upward (Fig. 2). However, the phyllic alteration is not well developed and sericite–quartz veins occur only in the local area.

Potassic alteration consisting of K-feldspathization and biotitization is dominated in the deep part of the granodiorite porphyry (Fig. 2) and is superimposed by argillic alteration. Secondary K-feldspar replaced mainly plagioclase and dispersive matrix. Albite reaction rim on the plagioclase often occurred as a result of Na precipitation during the process of K-feldspar metasomatism. K-feldspar alteration halos also occur at the edge of quartz-chalcopyrite-magnetite veins (A-type, Gustafson & Hunt, 1975). Additionally, the quartz–K-feldspar veinlets occur in the intrusive rocks. Secondary biotite replaces mainly primary hornblende and biotite. Quartz-biotite-chalcopyrite veins and biotite veinlets (EB type, Gustafson & Quiroga, 1995) are also present. Hydrothermal magnetite occurs in the potassic alteration zone, where chalcopyrite exists with magnetite. Petrographic observations suggest that magnetite formed at the same time as the chalcopyrite or earlier than it.

The argillic alteration zone contains mainly kaolinite, illite and muscovite, replacing plagioclase and chlorite replacing biotite. The quartz-chalcopyrite (present in the center of the vein) veins (B type, Gustafson & Hunt, 1975) and chalcopyrite veinlets occur in the argillic alteration.

The propylitic zone occurs mainly in the pre-mineral basaltic andesite. The main alteration minerals are epidote, chlorite and carbonate. Chlorite replaced the biotite phenocrysts along its rim, cleavage and center, while the pseudomorphs of biotite are occasionally retained. Carbonate, quartz, epidote and other minerals fill in the amygdales of basaltic rocks.

### 2.3 Mineralization characteristics

The Duobuza ore section (the northeastern ore section of the Duolong deposit) occurs in the granodiorite porphyry and the contact zone with the wall rock. It is constrained in an area of 100–400 m width and 1400 m length. The ore section strikes north 20°E and dips 65° to 80°S, 500 m deep. The proven amount of the resource is 2.7 Mt Cu with a grade of 0.94% and 13 t Au with 0.21 g $t^{-1}$ in the ore section. The mineralization changes gradually from stockwork veinlets-disseminated ore in the upper part of the orebody to sparsely disseminated ore at depth. The Cu content decreases downwards.

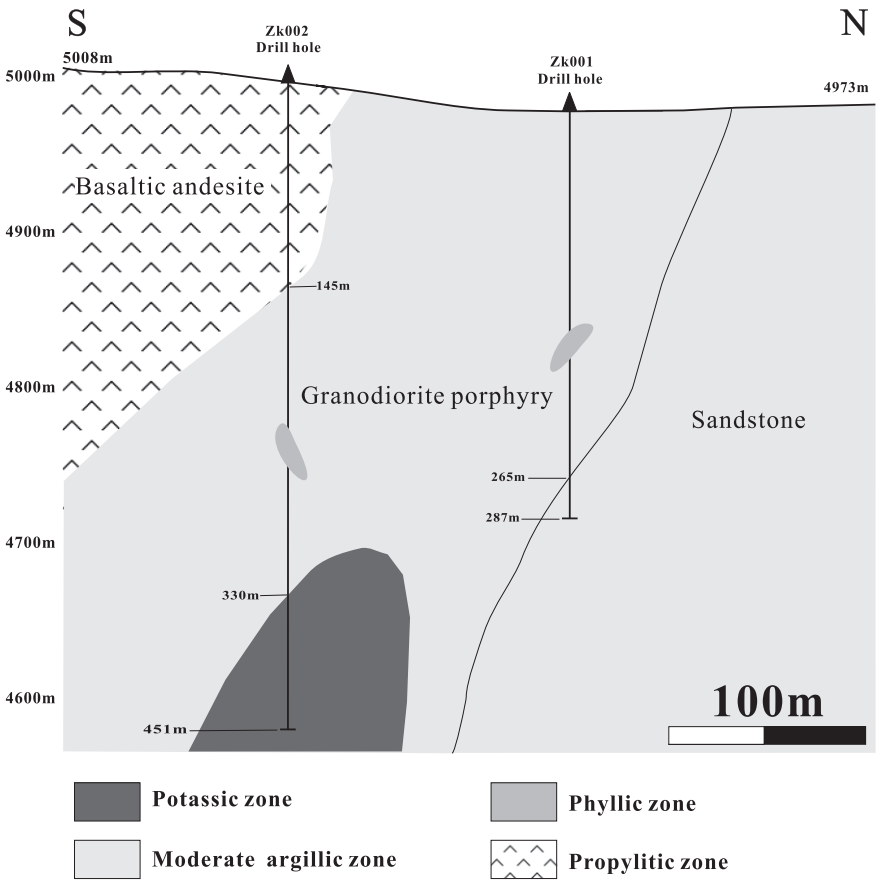


**Fig. 2** Cross-section of the Duolong gold-rich porphyry copper deposit, Tibet (modified from Li *et al*., 2007).

The Bolong ore section (the southwestern ore section of the Duolong deposit) is 900 m wide and 1000 m long on the surface, and its vertical extension is 600 m. A secondary oxidation enrichment zone is present in this section, and is composed mainly of malachite, azurite, limonite, chalcocite, native copper and cuprite. It is 70–100 m thick, and its average copper grade is greater than 1.17%, while an average Au grade is 0.28 g $t^{-1}$. The estimated copper and gold resources of the Bolong ore section are around 2.68 Mt with a mean grade of 0.5%, and around 28 t with a mean grade of 0.24 g $t^{-1}$, respectively. A preliminary analysis reveals a positive correlation between gold and copper (Li *et al*., 2007).

Hypogene minerals are mainly chalcopyrite and magnetite, followed by pyrite, hematite, rutile, and minor chalcocite, bornite and native gold. The amount of chalcopyrite is greater than that of bornite and far more than pyrite. Chalcopyrite occurs mainly as dissemination, stockwork and veinlets, while bornite occurs mainly in the form of exsolution in chalcopyrite (Fig. 3a). The gangue minerals are K-feldspar, albite, quartz, sericite, chlorite, carbonate, illite and gypsum. Molybdenite-quartz veins are rare (Fig. 3b). Hydrothermal magnetite is enriched in the Duolong deposit and contains chalcopyrite or coexists with it (Fig. 3c, d).

## 3. Samples and methods

Samples used in the present study were collected from four drill holes (ZK001, ZK002, ZK0802 and ZK1504) and from several outcrops in the Duolong deposit (Fig. 1b). Back-scattered electron images and chemical compositions of K-feldspar, albite, biotite, apatite, rutile and chlorite were acquired at the Institute of Geology and Geophysics, Chinese Academy of Sciences, using a JXA-8100 electron microprobe analyzer (EMPA) with a voltage of 15 kV, a beam current of 20 nA and a spot size of 5 μm. The compositions of magnetites and sulfides were analyzed using a Cameca SX-51 EMPA with a

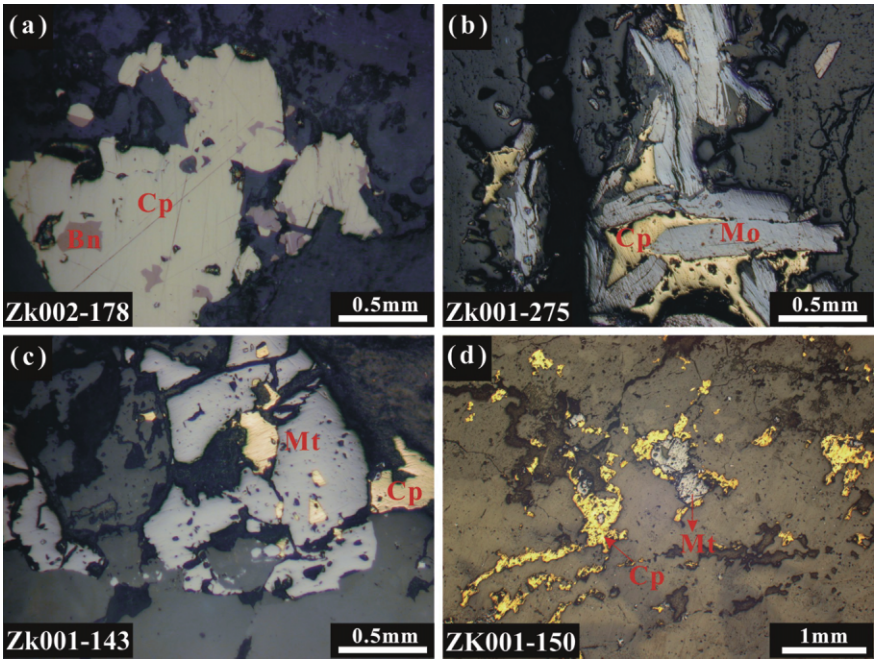


**Fig. 3** Photomicrographs of polished thin section under reflection light. (a) Bornite (Bn) exsolution from chalcopyrite; (b) quartz-chalcopyrite (Cp)-molybdenite (Mo) vein; (c) magnetite (Mt) associated with chalcopyrite and including chalcopyrite bleb; (d) magnetite (Mt) is associated with chalcopyrite.

voltage of 20 kV, a beam current of 15 nA and a spot size of 1 μm. The representative analyses of these minerals are given in Tables 1–8, respectively.

## 4. Results

Secondary albite replaces mainly plagioclase phenocrysts along their rims and fissures (Fig. 4a). The albite shows high contents of Ab (91.5–99.7%; Fig. 5; Table 2) with small amounts of An (0.2–8.2%) and Or (0.1–1.1%). They also show minor amounts of FeO (0–0.36%; Table 2).

Secondary K-feldspar replaces mainly plagioclase phenocrysts and occurs as veinlets (Fig. 4b). The K-feldspar shows high contents of Or (75.1–96.9%; Fig. 5; Table 1) with minor amounts of Ab (3.0–24.4%), FeO (0–0.44%; Table 1) and negligible An (0–0.6%).

Biotite occurs as phenocrysts, veinlets and dissemination. Biotite phenocrysts generally contain magnetite, rutile and apatite inclusions (Fig. 4c). Veinlet biotites are associated with magnetite, rutile and quartz (Fig. 4d). Disseminated biotites occur as fine-grained crystals within the groundmass of the granodiorite porphyry. Most of the biotite grains are partially chloritized. A total of 10 electron-microprobe biotite analyses were obtained from the potassic zone in the Duolong deposit. Representative biotite analyses are given in Table 3. According to the nomenclature of Foster (1960) for the classification of trioctahedral micas by chemical and lithological affinity, biotites are included in the Mg-rich biotites field ($X_{Mg}$ = 0.61–0.64) of the Mg–($Al^{VI}$+$Fe^{3+}$+Ti)–($Fe^{2+}$+Mn) ternary diagram (Fig. 6a). Biotite phenocrysts lie in the re-equilibrated primary biotite field of the 10 × $TiO_2$-$FeO_{total}$-MgO diagram (Fig. 6b, Nachit *et al*., 2005), suggesting their chemical compositions are possibly influenced by late-stage hydrothermal fluids. Moreover, the $SiO_2$, $Al_2O_3$, $Na_2O$ and CaO contents (Table 3) exhibit no significant differences between the biotite phenocrysts and veinlet biotites. All the biotites are absent of F. The biotite phenocrysts show slightly higher $TiO_2$, MgO, $K_2O$, Cl and MnO contents than the veinlet biotites (Fig. 7). This observation implies that the biotite phenocrysts may inherit the characters of primary magmatic biotite, in accordance with the magmatic biotite (higher MnO and $TiO_2$ content) from the Casino porphyry Cu-Au-Mo deposit, Yukon, Canada (Selby & Nesbitt, 2000).

As shown in the plot of $Fe^{3+}$-$Fe^{2+}$-Mg (Wones & Eugster, 1965), oxygen fugacity of these biotites is

**Table 1** Representative electron microprobe analysis results of K-feldspar in altered porphyries from the Duolong deposit

| Sample | ZK002-447 | ZK002-414 | ZK002-377 | ZK002-310 | ZK002-247 | ZK001-25 | ZK001-101 | ZK001-126 | DBZJ2-2 | |
|---|---|---|---|---|---|---|---|---|---|---|
| Analysis number | 4 | 6 | 4 | 9 | 5 | 7 | 4 | 7 | 8 | |
| Alteration zone | Potassic | | | | Argillic | | | | | |
| $SiO_2$ | 64.49 | 64.60 | 66.13 | 66.79 | 65.90 | 65.05 | 64.22 | 66.83 | 65.16 | 65.56 |
| $TiO_2$ | 0.01 | 0.00 | 0.00 | 0.01 | 0.01 | 0.01 | 0.00 | 0.00 | 0.02 | 0.00 |
| $Al_2O_3$ | 18.62 | 17.87 | 18.44 | 18.60 | 18.25 | 18.72 | 18.30 | 18.41 | 17.78 | 18.08 |
| $FeO_{total}$ | 0.44 | 0.02 | 0.10 | 0.22 | 0.01 | 0.11 | 0.22 | 0.01 | 0.15 | 0.14 |
| MnO | 0.00 | 0.04 | 0.01 | 0.02 | 0.01 | 0.00 | 0.02 | 0.00 | 0.03 | 0.00 |
| MgO | 0.01 | 0.00 | 0.00 | 0.05 | 0.01 | 0.00 | 0.00 | 0.00 | 0.00 | 0.06 |
| CaO | 0.00 | 0.07 | 0.01 | 0.00 | 0.00 | 0.10 | 0.01 | 0.00 | 0.01 | 0.00 |
| $Na_2O$ | 0.55 | 0.33 | 2.25 | 0.41 | 0.50 | 2.47 | 0.82 | 0.26 | 1.17 | 0.41 |
| $K_2O$ | 14.31 | 15.12 | 12.53 | 12.61 | 14.30 | 11.52 | 13.28 | 12.20 | 12.85 | 12.64 |
| F | 0.00 | 0.03 | 0.00 | 0.00 | 0.00 | 0.05 | 0.00 | 0.05 | 0.00 | 0.00 |
| Cl | 0.01 | 0.00 | 0.02 | 0.00 | 0.00 | 0.01 | 0.00 | 0.00 | 0.00 | 0.00 |
| Total | 98.44 | 98.10 | 99.53 | 98.74 | 98.98 | 98.02 | 96.89 | 97.75 | 97.18 | 96.92 |
| No. cations on the basis of 8 (O) | | | | | | | | | | |
| Si | 3.007 | 3.025 | 3.022 | 3.055 | 3.036 | 3.007 | 3.021 | 3.068 | 3.047 | 3.057 |
| Al | 1.024 | 0.986 | 0.993 | 1.003 | 0.991 | 1.020 | 1.015 | 0.996 | 0.980 | 0.994 |
| Ca | 0.000 | 0.004 | 0.001 | 0.000 | 0.000 | 0.005 | 0.000 | 0.000 | 0.000 | 0.000 |
| Na | 0.050 | 0.030 | 0.199 | 0.036 | 0.044 | 0.221 | 0.075 | 0.023 | 0.106 | 0.037 |
| K | 0.851 | 0.904 | 0.731 | 0.736 | 0.840 | 0.680 | 0.797 | 0.715 | 0.767 | 0.752 |
| An | 0.00 | 0.38 | 0.06 | 0.02 | 0.00 | 0.53 | 0.04 | 0.03 | 0.03 | 0.01 |
| Ab | 5.53 | 3.18 | 21.40 | 4.71 | 5.01 | 24.41 | 8.60 | 3.09 | 12.17 | 4.64 |
| Or | 94.47 | 96.44 | 78.54 | 95.27 | 94.99 | 75.06 | 91.36 | 96.88 | 87.80 | 95.35 |

**Table 2** Representative electron microprobe analysis results of albite in altered porphyries from the Duolong deposit

| Sample | ZK002-447 | ZK002-377 | ZK002-310 | ZK001-25 | ZK001-101 | ZK001-101 | DBZJ2-2 |
|---|---|---|---|---|---|---|---|
| Analysis number | 2 | 2 | 4 | 2 | 4 | 3 | 3 |
| Alteration zone | Potassic | | | Argillic | | | |
| $SiO_2$ | 67.63 | 66.91 | 67.89 | 68.17 | 66.91 | 68.89 | 66.61 |
| $TiO_2$ | 0.00 | 0.00 | 0.00 | 0.00 | 0.00 | 0.00 | 0.00 |
| $Al_2O_3$ | 19.87 | 21.23 | 20.77 | 20.27 | 20.56 | 19.91 | 21.08 |
| FeO | 0.36 | 0.05 | 0.02 | 0.03 | 0.03 | 0.01 | 0.00 |
| MnO | 0.00 | 0.00 | 0.03 | 0.01 | 0.00 | 0.01 | 0.00 |
| MgO | 0.00 | 0.00 | 0.00 | 0.00 | 0.00 | 0.00 | 0.00 |
| CaO | 1.43 | 1.45 | 0.54 | 0.21 | 1.37 | 0.24 | 1.63 |
| $Na_2O$ | 10.61 | 11.22 | 11.36 | 11.70 | 11.03 | 11.73 | 10.68 |
| $K_2O$ | 0.09 | 0.07 | 0.05 | 0.03 | 0.09 | 0.04 | 0.07 |
| F | 0.00 | 0.00 | 0.06 | 0.01 | 0.03 | 0.03 | 0.01 |
| Cl | 0.01 | 0.01 | 0.00 | 0.01 | 0.00 | 0.01 | 0.00 |
| Total | 99.99 | 100.92 | 100.66 | 100.43 | 99.99 | 100.82 | 100.08 |
| No. cations on the basis of 8 (O) | | | | | | | |
| Si | 2.969 | 2.912 | 2.950 | 2.968 | 2.935 | 2.985 | 2.918 |
| Al | 1.028 | 1.089 | 1.063 | 1.040 | 1.063 | 1.017 | 1.088 |
| Ca | 0.067 | 0.068 | 0.025 | 0.010 | 0.064 | 0.011 | 0.076 |
| Na | 0.903 | 0.947 | 0.957 | 0.987 | 0.938 | 0.985 | 0.907 |
| K | 0.005 | 0.004 | 0.003 | 0.002 | 0.005 | 0.002 | 0.004 |
| An | 6.9 | 6.6 | 2.6 | 1.0 | 6.4 | 1.1 | 7.7 |
| Ab | 92.6 | 93.0 | 97.2 | 98.9 | 93.1 | 98.7 | 91.9 |
| Or | 0.5 | 0.4 | 0.3 | 0.2 | 0.5 | 0.2 | 0.4 |

between the Ni-NiO (NNO) and $Fe_2O_3$-$Fe_3O_4$ (HM) (Fig. 6c), suggesting re-equilibrated biotite phenocrysts and veinlet biotites formed under a high oxidation condition. Biotite geothermometer proposed by Beane (1974) for hydrothermal biotites in the potassic alteration zone of the North American porphyry copper deposits is applied to biotites from the potassic zone of the Duolong deposit, where hydrothermal biotite coexists with magnetite and K-feldspar. Temperatures determined for the potassic zone lie within the range of 400 to 430°C (Fig. 8) with a mean value of 420°C, which is similar to the temperature range of that at Santa Rita (350–410°C), Dalli (400–450°C) and Galore Creek (450–550°C) (Beane, 1974).

Secondary chlorites occur extensively in all alteration zones, and replace biotite (Fig. 4e, g) and hornblende, and also occur in the chlorite-bearing veinlets (Fig. 4f). Chlorite compositions and calculated chemical formulae are listed in Table 4. In the classification of Hey (1954), chlorite corresponds mainly to pycnochlorite (Fig. 9). However, the chlorites from the wall rock (ZK0802-394) and a quartz-gypsum-carbonate-chlorite vein (ZK002-200) are plotted in the ripidolite and diabantite field, respectively. Chlorites generally have similar Fe/(Fe+Mg) ratios (0.30–0.45, Fig. 10), and Mn/(Mn+Mg) ratios (0.01–0.10) except for minor chlorites with higher ratios (Fig. 10). $Fe^{3+}/Fe^{2+}$ ratios of chlorites show negative correlation with $Al^{IV}$, and chlorites in the gypsum-carbonate-chlorite vein show highest $Fe^{3+}/Fe^{2+}$ ratios (0.22–0.23). Chlorites from the moderate argillic zone have higher $Fe^{3+}/Fe^{2+}$ ratios (0.01–0.11) than those from the potassic zone (0.02–0.09) and propylitic zone (0.02–0.10).

Chlorite geothermometry was used according to Cathelineau (1988) and Jowett (1991). The formation temperature of the chlorite from the Duolong deposit varies from 280°C to 360°C (Table 4), which is the same as that of a previous fluid inclusion study (Li *et al.*, 2007). The consistent formation temperatures of 280–360°C (Fig. 11) suggest that chlorite formed at the same temperature in all alteration zones. The formation temperature range of chlorite from the gypsum-carbonate-chlorite vein is between 190°C and 220°C, indicating it formed possibly in the later stage of hydrothermal activity.

Apatite occurs as inclusions in the biotite phenocrysts, single crystals in the veinlets and dissemination in each alteration zone. Apatite inclusions in the

**Table 3** Representative electron microprobe analyses of biotite from the potassic alteration zone in the Duolong deposit

| Sample | ZK002-447 | | | | | | | | | |
|---|---|---|---|---|---|---|---|---|---|---|
| Occurrence | Biotite phenocryst | | | | Biotite veinlet | | | | | |
| $SiO_2$ | 36.27 | 37.61 | 37.62 | 37.16 | 36.27 | 34.81 | 37.23 | 35.42 | 36.66 | 36.55 |
| $TiO_2$ | 3.84 | 3.22 | 3.77 | 3.86 | 3.23 | 3.29 | 3.37 | 2.97 | 3.55 | 3.14 |
| $Al_2O_3$ | 14.79 | 15.96 | 14.71 | 14.20 | 14.38 | 15.59 | 14.84 | 15.26 | 14.97 | 15.35 |
| $FeO_{total}$ | 14.81 | 16.37 | 15.86 | 15.42 | 15.54 | 16.53 | 15.45 | 15.94 | 16.09 | 16.04 |
| MnO | 0.17 | 0.34 | 0.17 | 0.20 | 0.32 | 0.54 | 0.26 | 0.69 | 0.62 | 0.50 |
| MgO | 14.55 | 14.32 | 14.35 | 14.53 | 13.99 | 14.92 | 15.42 | 15.36 | 14.83 | 14.75 |
| CaO | 0.00 | 0.09 | 0.00 | 0.01 | 0.04 | 0.12 | 0.00 | 0.01 | 0.12 | 0.03 |
| $Na_2O$ | 0.19 | 0.20 | 0.24 | 0.17 | 0.24 | 0.15 | 0.24 | 0.13 | 0.14 | 0.17 |
| $K_2O$ | 7.77 | 7.25 | 7.76 | 8.04 | 6.36 | 5.84 | 6.49 | 4.54 | 6.72 | 6.93 |
| F | 0.00 | 0.00 | 0.00 | 0.00 | 0.00 | 0.00 | 0.00 | 0.00 | 0.00 | 0.00 |
| Cl | 0.25 | 0.22 | 0.26 | 0.24 | 0.20 | 0.23 | 0.23 | 0.19 | 0.20 | 0.23 |
| $H_2O$* | 3.94 | 4.07 | 4.02 | 3.98 | 3.87 | 3.91 | 4.01 | 3.90 | 4.00 | 3.98 |
| F,Cl = O | 0.06 | 0.05 | 0.06 | 0.05 | 0.05 | 0.05 | 0.05 | 0.04 | 0.05 | 0.05 |
| Total | 96.52 | 99.59 | 98.70 | 97.75 | 94.40 | 95.88 | 97.49 | 94.38 | 97.84 | 97.62 |
| No. cations on the basis of 11 (O) | | | | | | | | | | |
| Si | 2.753 | 2.763 | 2.795 | 2.792 | 2.800 | 2.662 | 2.777 | 2.717 | 2.744 | 2.743 |
| $Al^{IV}$ | 1.247 | 1.237 | 1.205 | 1.208 | 1.200 | 1.338 | 1.223 | 1.283 | 1.256 | 1.257 |
| $Al^{VI}$ | 0.077 | 0.145 | 0.083 | 0.050 | 0.109 | 0.067 | 0.082 | 0.097 | 0.065 | 0.101 |
| Ti | 0.219 | 0.178 | 0.211 | 0.218 | 0.188 | 0.189 | 0.189 | 0.172 | 0.200 | 0.177 |
| $Fe^{(3+)}$* | 0.165 | 0.179 | 0.174 | 0.168 | 0.185 | 0.181 | 0.176 | 0.192 | 0.179 | 0.175 |
| $Fe^{2+}$ | 0.775 | 0.827 | 0.811 | 0.801 | 0.819 | 0.876 | 0.788 | 0.831 | 0.829 | 0.832 |
| Mn | 0.011 | 0.021 | 0.011 | 0.012 | 0.021 | 0.035 | 0.016 | 0.045 | 0.040 | 0.032 |
| Mg | 1.647 | 1.568 | 1.589 | 1.628 | 1.610 | 1.701 | 1.715 | 1.756 | 1.655 | 1.650 |
| Ca | 0.000 | 0.007 | 0.000 | 0.001 | 0.003 | 0.010 | 0.000 | 0.001 | 0.009 | 0.002 |
| Na | 0.028 | 0.028 | 0.035 | 0.025 | 0.035 | 0.022 | 0.035 | 0.019 | 0.020 | 0.024 |
| K | 0.752 | 0.680 | 0.736 | 0.771 | 0.626 | 0.570 | 0.618 | 0.445 | 0.642 | 0.664 |
| Total | 7.673 | 7.632 | 7.649 | 7.675 | 7.596 | 7.652 | 7.619 | 7.557 | 7.637 | 7.657 |
| OH* | 1.997 | 1.997 | 1.996 | 1.997 | 1.997 | 1.997 | 1.997 | 1.997 | 1.997 | 1.997 |
| F | 0.000 | 0.000 | 0.000 | 0.000 | 0.000 | 0.000 | 0.000 | 0.000 | 0.000 | 0.000 |
| Cl | 0.003 | 0.003 | 0.004 | 0.003 | 0.003 | 0.003 | 0.003 | 0.003 | 0.003 | 0.003 |
| $Al^{VI}+Fe^{3+}+Ti$ | 0.46 | 0.50 | 0.47 | 0.44 | 0.48 | 0.44 | 0.45 | 0.46 | 0.44 | 0.45 |
| $Fe^{2+}+Mn$ | 0.79 | 0.85 | 0.82 | 0.81 | 0.84 | 0.91 | 0.80 | 0.88 | 0.87 | 0.86 |
| $X_{Mg}$ | 0.64 | 0.61 | 0.62 | 0.63 | 0.62 | 0.62 | 0.64 | 0.63 | 0.62 | 0.62 |
| $X_{Fe}$ | 0.38 | 0.42 | 0.40 | 0.38 | 0.41 | 0.40 | 0.38 | 0.39 | 0.39 | 0.40 |
| $Fe^{3+}/Fe^{2+}$ | 0.21 | 0.22 | 0.21 | 0.21 | 0.23 | 0.21 | 0.22 | 0.23 | 0.22 | 0.21 |
| $\log(X_{Cl}/X_{OH})$ | −2.76 | −2.82 | −2.74 | −2.77 | −2.85 | −2.80 | −2.79 | −2.88 | −2.84 | −2.78 |
| IV(Cl) | −3.48 | −3.37 | −3.46 | −3.45 | −3.35 | −3.40 | −3.45 | −3.35 | −3.37 | −3.42 |
| $\log (fH_2O/fHCl)^{f\ luid}$ | 5.64 | 5.71 | 5.62 | 5.65 | 5.72 | 5.67 | 5.62 | 5.73 | 5.72 | 5.66 |
| Biotite geothermometer (°C) | 405 | 400 | 410 | 410 | 410 | 410 | 430 | 425 | 410 | 410 |

The $X_{Mg}$ ($X_{Mg}$ = Mg/Mg+Fe) and $X_{Fe}$ ($X_{Fe}$ = (Fe+$Al^{VI}$)/(Fe+Mg+$Al^{VI}$)) values are mole fractions of Mg and Fe (Zhu & Sverjensky, 1992). Ferric iron estimations are from Dymek (1983). Method of chlorine IV (Cl) intercept value is from Munoz (1984) as follow: IV (Cl) = –5.01–1.93$X_{Mg}$-log($X_{Cl}/X_{OH}$). The fugacity ratios of log ($fH_2O/fHCl$) $^{f\ luid}$ is calculated using the eauations by Munoz (1992) as follow: log ($fH_2O/fHCl$) $^{f\ luid}$ = 1000/T(1.15+0.55$X_{Mg}^{biotite}$)+0.68- log($X_{Cl}/X_{OH}$) $^{biotite}$, and T is the temperature in Kelvin of the halogen exchange. Calculating method for biotite geothermometer is from Beane (1974). * represents calculated value.

biotite phenocrysts are regarded as being of magmatic origin. Apatites show $SiO_2$ content of 0–3.27%, $TiO_2$ of 0–0.41%, $Al_2O_3$ of 0–0.77%, $K_2O$ of 0–0.22%, and no variation on these compositions of apatite in the biotite phenocrysts and other alteration zones (Table 5; Fig. 12). However, apatites from the moderate argillic zone show highest CaO content (54.8–56.9%), possibly suggesting the fluid is Ca-rich. In addition, apatites from the potassic zone have higher $Ce_2O_3$ content (0.08–0.48%) than those in the biotite phenocrysts and other alteration zones. The MnO content (Fig. 12) of apatite decreases from the potassic zone (0.36–0.82%), the biotite phenocrysts (0.25–0.46%), the propylitic zone (0.08–0.16%), to the argillic zone (0.01–0.42%).

**Table 4** Representative electron microprobe analysis results of chlorite from all alteration zones in the Duolong deposit

| Sample | ZK002-447 | ZK002-414 | ZK002-377 | ZK002-310 | ZK002-247 | ZK002-200 | ZK001-25 | ZK001-101 | ZK001-126 | 11906-2 | DBZJ2-2 | ZK0802-394 | ZK1502-387 | ZK002-200 | |
|---|---|---|---|---|---|---|---|---|---|---|---|---|---|---|---|
| Analysis number | 8 | 7 | 7 | 9 | 6 | 2 | 3 | 2 | 2 | 6 | 5 | 6 | 2 | 2 | |
| Alteration zone | Potassic | | | | Argillic | | | | | | | Propylitic | | Q-Gy-Cc-Chl vein | |
| $SiO_2$ | 28.28 | 28.16 | 27.48 | 28.70 | 29.50 | 27.85 | 27.37 | 25.82 | 27.04 | 28.43 | 28.44 | 25.66 | 26.67 | 30.72 | 33.17 |
| $TiO_2$ | 0.05 | 0.02 | 0.03 | 0.04 | 0.04 | 0.00 | 0.02 | 0.04 | 0.06 | 0.05 | 0.03 | 0.04 | 0.07 | 0.12 | 0.08 |
| $Al_2O_3$ | 19.32 | 19.90 | 20.71 | 18.24 | 20.78 | 20.14 | 19.89 | 19.54 | 20.37 | 20.45 | 19.51 | 21.52 | 20.03 | 21.22 | 21.40 |
| $FeO_{total}$ | 20.32 | 20.99 | 18.47 | 20.47 | 21.42 | 17.02 | 21.18 | 22.67 | 18.17 | 19.43 | 20.58 | 21.05 | 19.97 | 15.45 | 14.57 |
| MnO | 0.37 | 0.84 | 3.02 | 0.65 | 0.56 | 0.39 | 0.92 | 0.47 | 0.41 | 0.43 | 0.29 | 3.17 | 0.37 | 0.40 | 0.36 |
| MgO | 19.65 | 18.35 | 18.21 | 18.89 | 14.83 | 21.37 | 17.51 | 16.54 | 19.39 | 18.00 | 18.03 | 15.73 | 18.16 | 16.12 | 17.09 |
| CaO | 0.05 | 0.05 | 0.01 | 0.14 | 0.06 | 0.03 | 0.07 | 0.04 | 0.05 | 0.19 | 0.02 | 0.02 | 0.06 | 0.07 | 0.24 |
| $Na_2O$ | 0.00 | 0.01 | 0.07 | 0.04 | 0.01 | 0.03 | 0.01 | 0.06 | 0.03 | 0.02 | 0.02 | 0.04 | 0.00 | 0.04 | 0.05 |
| $K_2O$ | 0.01 | 0.00 | 0.02 | 0.01 | 0.39 | 0.00 | 0.04 | 0.01 | 0.04 | 0.06 | 0.05 | 0.04 | 0.05 | 0.42 | 0.89 |
| $Cr_2O_3$ | 0.10 | 0.15 | 0.01 | 0.38 | 0.05 | 0.20 | 0.05 | 0.05 | 0.15 | 0.04 | 0.12 | 0.07 | 0.19 | 0.11 | 0.35 |
| F | 0.00 | 0.00 | 0.00 | 0.00 | 0.00 | 0.00 | 0.00 | 0.00 | 0.00 | 0.00 | 0.00 | 0.00 | 0.00 | 0.00 | 0.00 |
| Cl | 0.00 | 0.00 | 0.02 | 0.01 | 0.00 | 0.01 | 0.01 | 0.00 | 0.01 | 0.01 | 0.01 | 0.00 | 0.00 | 0.01 | 0.00 |
| $H_2O$* | 11.80 | 11.80 | 11.75 | 11.70 | 11.80 | 11.84 | 11.57 | 11.17 | 11.58 | 11.78 | 11.70 | 11.43 | 11.44 | 11.82 | 12.38 |
| Total | 99.94 | 100.28 | 99.78 | 99.26 | 99.44 | 98.87 | 98.63 | 96.41 | 97.29 | 98.90 | 98.79 | 98.76 | 97.01 | 96.48 | 100.57 |
| No. cations on the basis of 14 (O) | | | | | | | | | | | | | | | |
| Si | 2.871 | 2.859 | 2.803 | 2.941 | 2.996 | 2.819 | 2.835 | 2.770 | 2.798 | 2.891 | 2.913 | 2.691 | 2.794 | 3.114 | 3.210 |
| $Al^{IV}$ | 1.129 | 1.141 | 1.197 | 1.059 | 1.004 | 1.181 | 1.165 | 1.230 | 1.202 | 1.109 | 1.087 | 1.309 | 1.206 | 0.886 | 0.790 |
| T site | 4.000 | 4.000 | 4.000 | 4.000 | 4.000 | 4.000 | 4.000 | 4.000 | 4.000 | 4.000 | 4.000 | 4.000 | 4.000 | 4.000 | 4.000 |
| $Al^{VI}$ | 1.183 | 1.239 | 1.292 | 1.143 | 1.483 | 1.223 | 1.263 | 1.242 | 1.282 | 1.343 | 1.268 | 1.350 | 1.267 | 1.650 | 1.651 |
| Ti | 0.004 | 0.002 | 0.002 | 0.003 | 0.003 | 0.000 | 0.002 | 0.003 | 0.004 | 0.004 | 0.003 | 0.003 | 0.005 | 0.009 | 0.006 |
| $Fe^{(3+)}$* | 0.069 | 0.103 | 0.081 | 0.099 | 0.240 | 0.053 | 0.094 | 0.010 | 0.083 | 0.165 | 0.147 | 0.043 | 0.078 | 0.235 | 0.222 |
| $Fe^{(2+)}$* | 1.657 | 1.679 | 1.495 | 1.655 | 1.579 | 1.388 | 1.740 | 2.024 | 1.489 | 1.487 | 1.615 | 1.803 | 1.672 | 1.075 | 0.958 |
| Mn | 0.032 | 0.072 | 0.261 | 0.056 | 0.048 | 0.033 | 0.081 | 0.042 | 0.036 | 0.037 | 0.025 | 0.281 | 0.033 | 0.035 | 0.029 |
| Mg | 2.974 | 2.777 | 2.769 | 2.885 | 2.245 | 3.225 | 2.703 | 2.646 | 2.990 | 2.729 | 2.753 | 2.459 | 2.836 | 2.436 | 2.465 |
| Ca | 0.005 | 0.006 | 0.001 | 0.015 | 0.007 | 0.003 | 0.008 | 0.005 | 0.006 | 0.021 | 0.002 | 0.002 | 0.007 | 0.007 | 0.025 |
| Na | 0.001 | 0.003 | 0.014 | 0.009 | 0.002 | 0.005 | 0.003 | 0.012 | 0.007 | 0.004 | 0.003 | 0.008 | 0.001 | 0.008 | 0.008 |
| K | 0.001 | 0.000 | 0.003 | 0.001 | 0.051 | 0.000 | 0.005 | 0.002 | 0.005 | 0.008 | 0.006 | 0.005 | 0.007 | 0.054 | 0.110 |
| Cr | 0.008 | 0.012 | 0.000 | 0.030 | 0.004 | 0.016 | 0.004 | 0.004 | 0.012 | 0.003 | 0.010 | 0.005 | 0.016 | 0.009 | 0.027 |
| M site | 5.932 | 5.893 | 5.918 | 5.896 | 5.662 | 5.947 | 5.904 | 5.991 | 5.914 | 5.801 | 5.833 | 5.959 | 5.921 | 5.518 | 5.499 |
| OH* | 4.000 | 4.000 | 4.000 | 4.000 | 4.000 | 4.000 | 4.000 | 4.000 | 4.000 | 4.000 | 4.000 | 4.000 | 4.000 | 4.000 | 4.000 |
| F | 0.000 | 0.000 | 0.000 | 0.000 | 0.000 | 0.000 | 0.000 | 0.000 | 0.000 | 0.000 | 0.000 | 0.000 | 0.000 | 0.000 | 0.000 |
| Cl | 0.000 | 0.000 | 0.000 | 0.000 | 0.000 | 0.000 | 0.000 | 0.000 | 0.000 | 0.000 | 0.000 | 0.000 | 0.000 | 0.000 | 0.000 |
| Fe/Fe+Mg | 0.37 | 0.39 | 0.36 | 0.38 | 0.45 | 0.31 | 0.40 | 0.43 | 0.34 | 0.38 | 0.39 | 0.43 | 0.38 | 0.35 | 0.32 |
| Mn/Mn+Mg | 0.01 | 0.03 | 0.09 | 0.02 | 0.02 | 0.01 | 0.03 | 0.02 | 0.01 | 0.01 | 0.01 | 0.10 | 0.01 | 0.01 | 0.01 |
| $Fe^{3+}/Fe^{2+}$ | 0.04 | 0.06 | 0.05 | 0.06 | 0.15 | 0.04 | 0.05 | 0.00 | 0.06 | 0.11 | 0.09 | 0.02 | 0.05 | 0.22 | 0.23 |
| Tem. 1 | 301 | 305 | 324 | 279 | 261 | 318 | 313 | 334 | 325 | 295 | 288 | 360 | 326 | 223 | 192 |
| Tem. 2 | 303 | 307 | 324 | 281 | 266 | 317 | 316 | 337 | 326 | 297 | 290 | 362 | 328 | 225 | 193 |

Q: quartz; Gy: gypsum; Cc: carbonate; Chl: chlorite; Tem: temperature. Chlorite recalculation with $Fe^{(3+)}$*, $Fe^{(2+)}$* and $H_2O$* estimation is carried out by Chlorite Formula Unit Calculator and Variety Namer Excel spreadsheet written by Tindle AG. Tem. 1 is calculated by T (°C) = 321.98 $Al^{IV}$/2–61.92 (Cathelineau, 1988); Tem. 2 is calculated by T (°C) = 319 $Al^{IV}{}_C$-69, $Al^{IV}{}_C = Al^{IV}/2+0.1(Fe/(Fe+Mg))$ (Jowett, 1991). *represents calculated value.

**Table 5** Representative electron microprobe analysis results of apatite from the Duolong deposit

| Sample | ZK002-447 | ZK002-447 | ZK002-338 | ZK001-150 | ZK001-101 | ZK3104-315 | |
|---|---|---|---|---|---|---|---|
| Analysis number | 3 | 4 | 3 | 4 | 3 | 7 | |
| Alteration zone | In the biotite phenocryst | Potassic | | Moderate argillic | | Propylitic | |
| $P_2O_5$ | 41.58 | 43.26 | 43.26 | 39.84 | 42.95 | 42.72 | 39.62 |
| $SiO_2$ | 1.26 | 0.00 | 0.22 | 0.22 | 0.06 | 0.19 | 3.27 |
| $SO_3$ | 0.82 | 0.10 | 0.12 | 0.17 | 0.03 | 0.01 | 0.04 |
| $TiO_2$ | 0.09 | 0.07 | 0.03 | 0.06 | 0.01 | 0.13 | 0.07 |
| $Al_2O_3$ | 0.08 | 0.00 | 0.00 | 0.01 | 0.00 | 0.03 | 0.77 |
| $Ce_2O_3$ | 0.14 | 0.24 | 0.30 | 0.09 | 0.05 | 0.22 | 0.03 |
| CaO | 53.68 | 53.98 | 53.83 | 57.91 | 55.10 | 54.45 | 53.21 |
| MnO | 0.46 | 0.36 | 0.59 | 0.00 | 0.42 | 0.16 | 0.13 |
| FeO | 0.80 | 0.27 | 0.46 | 0.54 | 0.39 | 0.66 | 0.87 |
| $Na_2O$ | 0.19 | 0.16 | 0.14 | 0.00 | 0.11 | 0.03 | 0.04 |
| $K_2O$ | 0.07 | 0.00 | 0.00 | 0.14 | 0.00 | 0.22 | 0.21 |
| F | 1.60 | 1.51 | 1.53 | 1.80 | 1.58 | 1.47 | 1.43 |
| Cl | 1.00 | 1.30 | 1.25 | 0.00 | 1.05 | 1.43 | 1.59 |
| F,Cl = O | 0.90 | 0.93 | 0.93 | 0.76 | 0.90 | 0.94 | 0.96 |
| Total | 100.86 | 100.32 | 100.81 | 100.02 | 100.86 | 100.78 | 100.33 |
| No. cations on the basis of 25 (O) | | | | | | | |
| P | 5.682 | 5.944 | 5.920 | 5.594 | 5.889 | 5.874 | 5.459 |
| Si | 0.203 | 0.000 | 0.036 | 0.037 | 0.009 | 0.030 | 0.532 |
| S | 0.100 | 0.012 | 0.014 | 0.021 | 0.004 | 0.001 | 0.005 |
| Ti | 0.010 | 0.008 | 0.004 | 0.008 | 0.001 | 0.015 | 0.009 |
| Al | 0.014 | 0.000 | 0.000 | 0.002 | 0.000 | 0.006 | 0.148 |
| Ce | 0.008 | 0.015 | 0.018 | 0.005 | 0.003 | 0.013 | 0.002 |
| Ca | 9.283 | 9.387 | 9.322 | 10.292 | 9.562 | 9.475 | 9.278 |
| Mn | 0.063 | 0.050 | 0.081 | 0.000 | 0.058 | 0.022 | 0.018 |
| Fe | 0.108 | 0.036 | 0.062 | 0.075 | 0.053 | 0.089 | 0.118 |
| Na | 0.061 | 0.051 | 0.044 | 0.000 | 0.036 | 0.010 | 0.012 |
| K | 0.014 | 0.000 | 0.001 | 0.029 | 0.001 | 0.047 | 0.043 |
| F | 0.815 | 0.775 | 0.782 | 0.943 | 0.808 | 0.758 | 0.736 |
| Cl | 0.272 | 0.357 | 0.343 | 0.000 | 0.288 | 0.394 | 0.439 |
| OH* | 0.913 | 0.868 | 0.875 | 1.056 | 0.904 | 0.848 | 0.825 |

*represents calculated value.

FeO content of apatite decreases from the propylitic zone (0.52–0.87%), the biotite phenocrysts (0.20–0.87%), the potassic zone (0.27–0.88%), to the argillic zone (0–0.54%).

Apatite inclusions in the biotite phenocrysts show highest $Na_2O$ content (0.18–0.35%). Apatites in the potassic zone have higher $Na_2O$ content (0.10–0.16%) than the moderate argillic zone (0.00–0.11%) and the propylitic zone (0.03–0.08%). All apatites analyzed show Cl abundance between 0 and 2.29%, highest Cl content (1.04–2.29%) and lowest F content (1.26–1.57%) in the propylitic zone, lowest Cl (0–1.05%) and highest F (1.58–1.85%) in the argillic zone. Apatite inclusions in the biotite phenocrysts have higher Cl content (1–1.37%) and lower F content (1.46–1.60%). Apatite inclusions in the biotite phenocrysts show higher $SO_3$ content (0.44–0.82%) than apatite in the potassic zone (0.04–0.17%) and the moderate argillic zone (0.03–0.17%). Apatite in the propylitic zone has the lowest $SO_3$ content (0–0.04%).

Magnetite occurs as an inclusion in the biotite phenocryst (Fig. 4e), veinlet magnetite and disseminated magnetite (Figs 3d, 4a). The representative results of magnetite are presented in Table 6. Magnetite shows $Fe_2O_3$ content of 63.9–68.8%, FeO of 28.1–32.4%, $TiO_2$ of 0–1.39%, $Al_2O_3$ of 0–1.19%, $Cr_2O_3$ of 0–3.15%, MnO of 0–0.70%, and minor amounts of CaO, MgO, CuO and NiO. The highest $Cr_2O_3$ content (1.06–3.15%) of magnetite from the propylitic zone may be caused by the high Cr content of basaltic rocks. Magnetite from the potassic zone has higher $TiO_2$ content than that in the argillic zone, possibly suggesting a higher formation temperature of magnetite in the potassic zone.

**Table 6** Representative electron microprobe analysis results of magnetite from the Duolong deposit

| Sample | ZK002-447 | | ZK002-338 | ZK001-150 | | ZK001-101 | | ZK001-25 | | ZK3104-315 | | ZK0802-394 |
|---|---|---|---|---|---|---|---|---|---|---|---|---|
| Alteration zone | Potassic | | | Argillic | | | | | | Propylitic | | |
| Occurrences | Disseminated | | | Disseminated | A-type veinlet | In the biotite | Disseminated | | Mt-bearing veinlet | Mt-bearing veinlet | Disseminated | |
| $SiO_2$ | 0.03 | 0.04 | 0.05 | 0.21 | 0.13 | 0.00 | 0.06 | 0.03 | 0.06 | 0.11 | 0.28 | 0.10 |
| $TiO_2$ | 0.55 | 0.61 | 0.56 | 0.14 | 0.13 | 0.00 | 0.36 | 0.18 | 0.18 | 0.16 | 0.74 | 0.71 |
| $Al_2O_3$ | 0.71 | 0.78 | 0.87 | 0.47 | 0.26 | 0.45 | 0.36 | 0.34 | 0.32 | 0.04 | 0.17 | 0.28 |
| $Cr_2O_3$ | 0.03 | 0.02 | 0.06 | 0.06 | 0.08 | 0.04 | 0.03 | 0.06 | 0.06 | 2.74 | 1.77 | 1.20 |
| $Fe_2O_3$ | 67.01 | 66.97 | 66.92 | 66.81 | 66.98 | 68.42 | 68.14 | 68.21 | 67.57 | 65.80 | 65.29 | 65.16 |
| MgO | 0.09 | 0.06 | 0.08 | 0.00 | 0.01 | 0.00 | 0.02 | 0.01 | 0.02 | 0.03 | 0.09 | 0.02 |
| CaO | 0.00 | 0.01 | 0.04 | 0.01 | 0.01 | 0.00 | 0.00 | 0.02 | 0.02 | 0.00 | 0.04 | 0.07 |
| MnO | 0.09 | 0.09 | 0.16 | 0.15 | 0.16 | 0.00 | 0.02 | 0.14 | 0.13 | 0.13 | 0.08 | 0.25 |
| FeO | 31.40 | 31.59 | 31.45 | 30.51 | 30.42 | 31.12 | 31.53 | 31.12 | 30.81 | 31.04 | 31.43 | 31.07 |
| NiO | 0.03 | 0.03 | 0.01 | 0.01 | 0.02 | 0.00 | 0.08 | 0.02 | 0.01 | 0.02 | 0.03 | 0.01 |
| CuO | 0.01 | 0.02 | 0.00 | 0.01 | 0.00 | 0.00 | 0.00 | 0.06 | 0.05 | 0.03 | 0.02 | 0.09 |
| Total | 99.96 | 100.23 | 100.21 | 98.39 | 98.20 | 100.03 | 100.60 | 100.18 | 99.22 | 100.09 | 99.94 | 98.97 |
| No. cations on the basis of 32 (O) | | | | | | | | | | | | |
| Si | 0.011 | 0.013 | 0.015 | 0.065 | 0.060 | 0.000 | 0.020 | 0.010 | 0.017 | 0.034 | 0.084 | 0.031 |
| Ti | 0.126 | 0.141 | 0.128 | 0.032 | 0.030 | 0.000 | 0.084 | 0.041 | 0.042 | 0.038 | 0.170 | 0.166 |
| Al | 0.258 | 0.281 | 0.313 | 0.173 | 0.100 | 0.165 | 0.130 | 0.122 | 0.116 | 0.014 | 0.060 | 0.103 |
| Cr | 0.006 | 0.005 | 0.014 | 0.015 | 0.036 | 0.009 | 0.007 | 0.014 | 0.014 | 0.664 | 0.426 | 0.295 |
| Fe | 15.464 | 15.405 | 15.383 | 15.671 | 15.726 | 15.826 | 15.659 | 15.745 | 15.742 | 15.200 | 14.988 | 15.189 |
| Mg | 0.041 | 0.027 | 0.037 | 0.002 | 0.009 | 0.000 | 0.009 | 0.003 | 0.009 | 0.013 | 0.039 | 0.009 |
| Ca | 0.001 | 0.004 | 0.014 | 0.004 | 0.007 | 0.000 | 0.001 | 0.006 | 0.007 | 0.001 | 0.013 | 0.022 |
| Mn | 0.024 | 0.024 | 0.041 | 0.038 | 0.045 | 0.000 | 0.005 | 0.035 | 0.033 | 0.033 | 0.019 | 0.066 |
| Fe | 8.051 | 8.076 | 8.034 | 7.954 | 7.937 | 8.000 | 8.052 | 7.983 | 7.978 | 7.970 | 8.018 | 8.050 |
| Ni | 0.007 | 0.008 | 0.003 | 0.003 | 0.004 | 0.000 | 0.019 | 0.005 | 0.003 | 0.005 | 0.008 | 0.002 |
| Cu | 0.002 | 0.004 | 0.001 | 0.002 | 0.000 | 0.000 | 0.000 | 0.015 | 0.012 | 0.006 | 0.006 | 0.022 |
| Total | 23.993 | 23.987 | 23.983 | 23.959 | 23.952 | 24.000 | 23.985 | 23.978 | 23.973 | 23.977 | 23.830 | 23.954 |

**Table 7** Representative electron microprobe analyses results of rutile from the Duolong deposit

| Sample | ZK002-447 | | | ZK002-338 | | ZK001-25 | | | ZK001-150 | | | ZK001-101 | | |
|---|---|---|---|---|---|---|---|---|---|---|---|---|---|---|
| Alteration zone | Potassic | | | | | Argillic | | | | | | | | |
| Occurrences | Rut-Bio | Rut | Rut | Rut-Bio | Rut | Rut | Rut | Rut | Rut-A | Rut-A | Rut | Rut | Rut | Rut |
| $SiO_2$ | 2.28 | 1.27 | 2.11 | 1.64 | 0.34 | 0.76 | 0.32 | 0.13 | 0.08 | 0.04 | 0.72 | 1.53 | 0.85 | 1.78 |
| $TiO_2$ | 90.88 | 93.33 | 92.17 | 91.73 | 96.35 | 96.28 | 97.50 | 98.24 | 95.80 | 97.08 | 95.12 | 92.50 | 93.54 | 95.74 |
| $Al_2O_3$ | 1.14 | 0.41 | 0.96 | 0.63 | 0.10 | 0.21 | 0.03 | 0.01 | 0.03 | 0.00 | 0.32 | 0.70 | 0.29 | 0.52 |
| $V_2O_3$ | 0.89 | 0.75 | 0.62 | 0.65 | 0.58 | 0.49 | 0.46 | 0.59 | 1.13 | 0.90 | 0.62 | 0.62 | 0.72 | 0.77 |
| $Cr_2O_3$ | 0.19 | 0.30 | 0.36 | 0.14 | 0.06 | 0.15 | 0.10 | 0.11 | 0.04 | 0.04 | 0.08 | 0.15 | 0.21 | 0.00 |
| MgO | 0.10 | 0.00 | 0.72 | 0.00 | 0.00 | 0.00 | 0.00 | 0.00 | 0.00 | 0.00 | 0.00 | 0.46 | 0.00 | 0.03 |
| CaO | 0.21 | 0.45 | 0.84 | 2.71 | 0.11 | 0.05 | 0.07 | 0.05 | 0.17 | 0.18 | 0.41 | 0.21 | 1.13 | 0.08 |
| MnO | 0.17 | 0.14 | 0.04 | 0.08 | 0.08 | 0.03 | 0.00 | 0.00 | 0.00 | 0.00 | 0.01 | 0.02 | 0.00 | 0.00 |
| FeO | 1.86 | 1.45 | 1.57 | 1.04 | 1.03 | 1.12 | 0.54 | 1.02 | 1.25 | 1.14 | 1.14 | 1.81 | 2.08 | 0.75 |
| NiO | 0.05 | 0.01 | 0.00 | 0.01 | 0.02 | 0.07 | 0.02 | 0.04 | 0.00 | 0.00 | 0.00 | 0.03 | 0.02 | 0.03 |
| CuO | 0.03 | 0.08 | 0.00 | 0.06 | 0.00 | 0.01 | 0.16 | 0.14 | 0.56 | 0.01 | 0.00 | 0.12 | 0.00 | 0.01 |
| SnO | 0.00 | 0.04 | 0.04 | 0.04 | 0.06 | 0.05 | 0.01 | 0.06 | 0.05 | 0.08 | 0.00 | 0.01 | 0.04 | 0.00 |
| $Na_2O$ | 0.10 | 0.03 | 0.06 | 0.19 | 0.02 | 0.00 | 0.00 | 0.11 | 0.02 | 0.02 | 0.02 | 0.23 | 0.06 | 0.02 |
| $K_2O$ | 0.20 | 0.12 | 0.05 | 0.11 | 0.04 | 0.33 | 0.26 | 0.25 | 0.01 | 0.00 | 0.03 | 0.05 | 0.05 | 0.49 |
| total | 98.11 | 98.37 | 99.55 | 99.02 | 98.78 | 99.56 | 99.48 | 100.73 | 99.15 | 99.49 | 98.48 | 98.46 | 98.99 | 100.22 |
| No. cations on the basis of 2 (O) | | | | | | | | | | | | | | |
| Si | 0.031 | 0.017 | 0.028 | 0.022 | 0.005 | 0.010 | 0.004 | 0.002 | 0.001 | 0.001 | 0.010 | 0.021 | 0.012 | 0.024 |
| Ti | 0.930 | 0.956 | 0.930 | 0.936 | 0.981 | 0.973 | 0.985 | 0.984 | 0.978 | 0.984 | 0.971 | 0.945 | 0.957 | 0.957 |
| Al | 0.018 | 0.007 | 0.015 | 0.010 | 0.002 | 0.003 | 0.001 | 0.000 | 0.000 | 0.000 | 0.005 | 0.011 | 0.005 | 0.008 |
| V | 0.010 | 0.008 | 0.007 | 0.007 | 0.006 | 0.005 | 0.005 | 0.006 | 0.012 | 0.010 | 0.007 | 0.007 | 0.008 | 0.008 |
| Cr | 0.002 | 0.003 | 0.004 | 0.002 | 0.001 | 0.002 | 0.001 | 0.001 | 0.000 | 0.001 | 0.001 | 0.002 | 0.002 | 0.000 |
| Mg | 0.002 | 0.000 | 0.014 | 0.000 | 0.000 | 0.000 | 0.000 | 0.000 | 0.000 | 0.000 | 0.000 | 0.009 | 0.000 | 0.001 |
| Ca | 0.003 | 0.007 | 0.012 | 0.039 | 0.002 | 0.001 | 0.001 | 0.001 | 0.002 | 0.003 | 0.006 | 0.003 | 0.017 | 0.001 |
| Mn | 0.002 | 0.002 | 0.001 | 0.001 | 0.001 | 0.000 | 0.000 | 0.000 | 0.000 | 0.000 | 0.000 | 0.000 | 0.000 | 0.000 |
| Fe | 0.021 | 0.017 | 0.018 | 0.012 | 0.012 | 0.013 | 0.006 | 0.011 | 0.014 | 0.013 | 0.013 | 0.021 | 0.024 | 0.008 |
| Ni | 0.001 | 0.000 | 0.000 | 0.000 | 0.000 | 0.001 | 0.000 | 0.000 | 0.000 | 0.000 | 0.000 | 0.000 | 0.000 | 0.000 |
| Cu | 0.000 | 0.001 | 0.000 | 0.001 | 0.000 | 0.000 | 0.002 | 0.001 | 0.006 | 0.000 | 0.000 | 0.001 | 0.000 | 0.000 |
| Sn | 0.000 | 0.000 | 0.000 | 0.000 | 0.000 | 0.000 | 0.000 | 0.000 | 0.000 | 0.001 | 0.000 | 0.000 | 0.000 | 0.000 |
| Na | 0.003 | 0.001 | 0.002 | 0.005 | 0.000 | 0.000 | 0.000 | 0.003 | 0.001 | 0.001 | 0.001 | 0.006 | 0.002 | 0.001 |
| K | 0.004 | 0.002 | 0.001 | 0.002 | 0.001 | 0.006 | 0.005 | 0.004 | 0.000 | 0.000 | 0.001 | 0.001 | 0.001 | 0.008 |
| total | 1.027 | 1.020 | 1.031 | 1.036 | 1.010 | 1.014 | 1.010 | 1.014 | 1.015 | 1.011 | 1.014 | 1.028 | 1.026 | 1.016 |

Rut-Bio: rutile in the biotite; Rut-A: rutile in the A-type vein; Rut: rutile.

**Table 8** Representative electron microprobe analysis results of sulfides from the Duolong deposit

| Sample | ZK002-447 | ZK002-219 | | ZK002-178 | | ZK001-25 | | ZK001-85 | | ZK001-98 | |
|---|---|---|---|---|---|---|---|---|---|---|---|
| Minerals | Cp | Py | Cp | Cp-Bn | Bn-Cp | Cp-A | Cp | Bn-Cp | Cp-Bn | Cp-Mo | Cp |
| Fe | 30.20 | 46.33 | 30.23 | 30.40 | 10.98 | 29.90 | 30.65 | 11.03 | 30.15 | 29.94 | 30.04 |
| S | 34.55 | 53.36 | 34.72 | 34.85 | 26.13 | 34.72 | 35.04 | 25.20 | 35.10 | 35.24 | 34.45 |
| Cu | 34.62 | 0.04 | 34.53 | 34.06 | 62.85 | 34.67 | 34.10 | 63.12 | 33.98 | 34.35 | 34.60 |
| Zn | 0.11 | 0.01 | 0.08 | 0.02 | 0.05 | 0.00 | 0.00 | 0.05 | 0.00 | 0.00 | 0.00 |
| As | 0.00 | 0.08 | 0.04 | 0.05 | 0.03 | 0.37 | 0.40 | 0.40 | 0.37 | 0.25 | 0.39 |
| Se | 0.03 | 0.03 | 0.03 | 0.02 | 0.00 | 0.05 | 0.06 | 0.07 | 0.07 | 0.05 | 0.03 |
| Ag | 0.08 | 0.02 | 0.08 | 0.12 | 0.16 | 0.07 | 0.03 | 0.08 | 0.18 | 0.11 | 0.05 |
| Te | 0.07 | 0.01 | 0.09 | 0.00 | 0.01 | 0.03 | 0.03 | 0.08 | 0.03 | 0.01 | 0.07 |
| Pb | 0.00 | 0.00 | 0.00 | 0.00 | 0.00 | 0.00 | 0.00 | 0.00 | 0.00 | 0.00 | 0.00 |
| Bi | 0.13 | 0.14 | 0.10 | 0.10 | 0.09 | 0.00 | 0.10 | 0.00 | 0.11 | 0.03 | 0.10 |
| Total | 99.80 | 100.02 | 99.90 | 99.62 | 100.30 | 100.21 | 100.77 | 100.03 | 99.99 | 99.98 | 99.73 |

| Sample | ZK001-150 | | | ZK1502-432 | | ZK3104-315 | | | | ZK0802-336 | |
|---|---|---|---|---|---|---|---|---|---|---|---|
| Minerals | Cp-A | Py-Mt | Cp-Mt | Cp-V | Py-V | Cp-Mt | Cp-Py | Py-Cp | Py | Cp | Py |
| Fe | 29.80 | 46.69 | 30.39 | 30.29 | 46.54 | 30.69 | 30.51 | 46.3 | 46.57 | 30.42 | 46.41 |
| S | 34.97 | 53.16 | 34.43 | 34.59 | 52.9 | 34.85 | 34.84 | 52.79 | 52.89 | 34.73 | 53.73 |
| Cu | 34.19 | 0.00 | 34.37 | 34.45 | 0.00 | 33.99 | 33.99 | 0.00 | 0.00 | 34.36 | 0.00 |
| Zn | 0.00 | 0.00 | 0.00 | 0.13 | 0.05 | 0.00 | 0.00 | 0.00 | 0.00 | 0.00 | 0.00 |
| As | 0.36 | 0.33 | 0.38 | 0.05 | 0.05 | 0.35 | 0.33 | 0.39 | 0.33 | 0.17 | 0.06 |
| Se | 0.04 | 0.06 | 0.03 | 0.05 | 0.06 | 0.00 | 0.01 | 0.04 | 0.04 | 0.05 | 0.05 |
| Ag | 0.00 | 0.08 | 0.01 | 0.04 | 0.12 | 0.00 | 0.10 | 0.15 | 0.03 | 0.07 | 0.10 |
| Te | 0.00 | 0.00 | 0.06 | 0.12 | 0.04 | 0.04 | 0.04 | 0.00 | 0.00 | 0.00 | 0.00 |
| Pb | 0.00 | 0.00 | 0.00 | 0.00 | 0.00 | 0.00 | 0.00 | 0.00 | 0.00 | 0.00 | 0.00 |
| Bi | 0.16 | 0.23 | 0.11 | 0.07 | 0.20 | 0.06 | 0.08 | 0.19 | 0.21 | 0.15 | 0.18 |
| Total | 99.52 | 100.55 | 99.78 | 99.79 | 99.96 | 99.98 | 99.9 | 99.86 | 100.07 | 99.95 | 100.53 |

Cp-A: chalcopyrite in the A-type veinlet; Bn-Cp: bornite exsolution from chalcopyrite; Cp-Bn: chalcopyrite containing bornite; Cp-Mo: chalcopyrite in quartz-chalcopyrite-molybdenite vein; Cp/Py-V: chalcopyrite in quartz-pyrite-chalcopyrite vein; Py-Cp: pyrite containing chalcopyrite; Cp/Py-Mt: chalcopyrite/pyrite in magnetite.

Rutile occurs mainly as inclusions in biotite phenocrysts, and is closely associated with chloritized biotite (Fig. 4e, h) in the potassic and argillic zones of the altered granodiorite porphyry. The representative results of rutile analysis are presented in Table 7. These results indicate that rutile ($TiO_2$ content of 90.9–98.2%) is relatively enriched in $SiO_2$ (0.04–2.28%), $V_2O_3$ (0.46–1.13%), CaO (0.05–2.71%), and FeO (0.54–2.28%). They show minor amounts of $Al_2O_3$ (up to 1.14%). $SiO_2$ and $Al_2O_3$ of rutile show negative correlation with $TiO_2$. Other element contents of rutile show no significant difference among all the alteration zones. The high $V_2O_3$ content (0.46–1.13%) of rutile in the Duolong deposit is similar with rutile ($V_2O_3$ >0.4%) from mineralized samples of the Northparkes porphyry Cu-Au deposit, New South Wales, Australia (Scott, 2005).

Sulfides are mainly chalcopyrite and pyrite, followed by minor bornite, native gold and molybdenite. Chalcopyrite, pyrite and bornite show compositions close to their ideal composition ($CuFeS_2$, $FeS_2$, $Cu_5FeS_4$, respectively), as presented in Table 8.

## 5. Discussion

### 5.1 Variations of T and $fO_2$ during magmatic-hydrothermal evolution

The highest $SO_3$ content (0.44–0.82%) of apatite inclusions in the biotite phenocrysts indicates a high oxidation state of magma (Streck & Dilles, 1998; Parat *et al.*, 2002; Imai, 2004). Re-equilibrated biotite phenocrysts (Fig. 6b) and biotites in the veins from the potassic zone formed in the temperature range of 400–430°C. Abundant hydrothermal magnetite occurs in the potassic zone, also indicating the high oxygen fugacity of ore-forming fluid. However, apatites in the potassic zone show lower $SO_3$ (0.04–0.17%) than apatite inclusions in the biotite phenocrysts. This observation suggests that the partitioning of $SO_3$ between apatite and melt may have been different

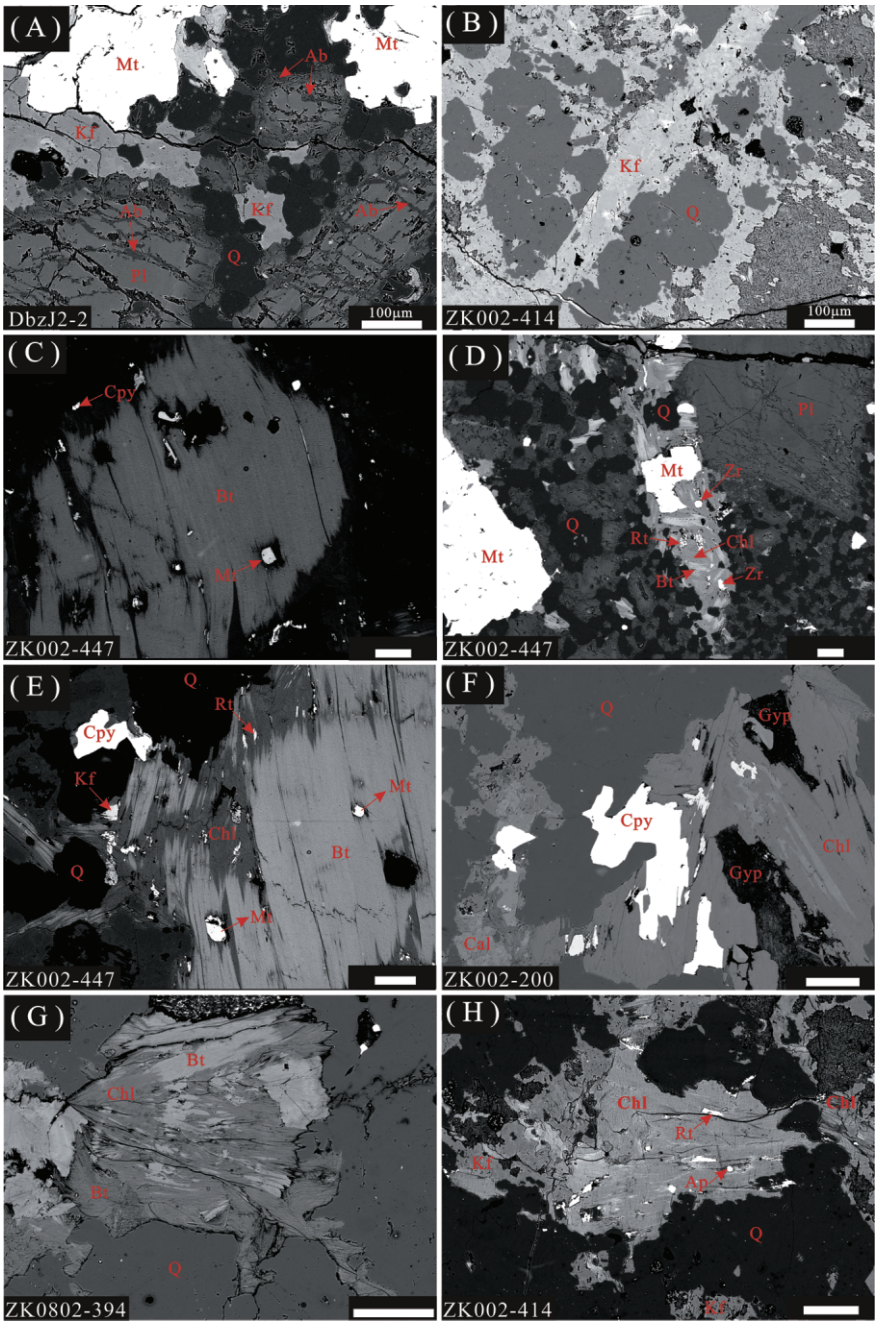


**Fig. 4** Back-scattered electron images showing: (a) albite replaces plagioclase phenocryst along its rim and fissures. The assemblage of quartz + magnetite + K-feldspar occurs later; (b) K-feldspar occurs as a veinlet; (c) biotite phenocryst contains magnetite. (d) biotite in the veinlet is associated with magnetite, rutile, zircon and quartz. Minor chlorite replaces the biotite. (e) Biotite phenocryst contains magnetite and rutile, and was replaced by the chlorite; (f) chlorite occurs in the quartz-chlorite-gypsum-carbonate-chalcopyrite vein. And chlorite was associated with gypsum; (g) replacement of secondary biotite by chlorite; (h) secondary chlorite associated with quartz, K-feldspar, apatite and rutile. Abbreviations: Kf = K-feldspar; Ap = apatite; Rt = rutile; Chl = chlorite; Bt = biotite; Q = quartz; Cpy = chalcopyrite; Mt = magnetite; Ab = albite; Pl = plagioclase; Zr = zircon; Gyp = gypsum; Cal = carbonate.

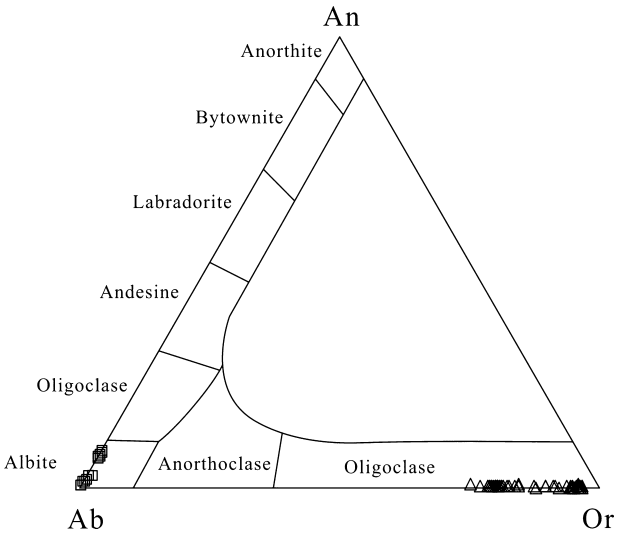


**Fig. 5** Ternary classification diagram Ab-An-Or for feldspars, showing the chemical variability of secondary K-feldspar and albite.

from that between apatite and ore-forming hydrothermal fluid.

The temperature range of 280–360°C for chlorite formation suggests that chlorites formed at similar temperatures in all alteration zones, except for chlorite from the gypsum-carbonate-chlorite vein, of which the calculated formation temperature is between 190°C and 220°C.

$Fe^{3+}/Fe^{2+}$ ratio of mineral is a good indicator of the oxygen fugacity of ore-forming fluid. $Fe^{3+}/Fe^{2+}$ ratios of chlorites are negatively correlated with $Al^{IV}$ (Fig. 13a), and chlorites in the quartz-gypsum-carbonate-chlorite vein show highest $Fe^{3+}/Fe^{2+}$ ratios (0.22–0.23), in accordance with coexisting gypsum (Fig. 4f). Chlorites from the argillic zone have higher $Fe^{3+}/Fe^{2+}$ ratios (0.01–0.11) than the potassic zone (0.02–0.09) and propylitic zone (0.02–0.10). This observation suggests the oxygen fugacity of ore-forming fluid increases toward the late ore-forming stage (Fig. 13b). The elevated oxygen fugacity of ore-forming fluid may result from sulfide precipitation:

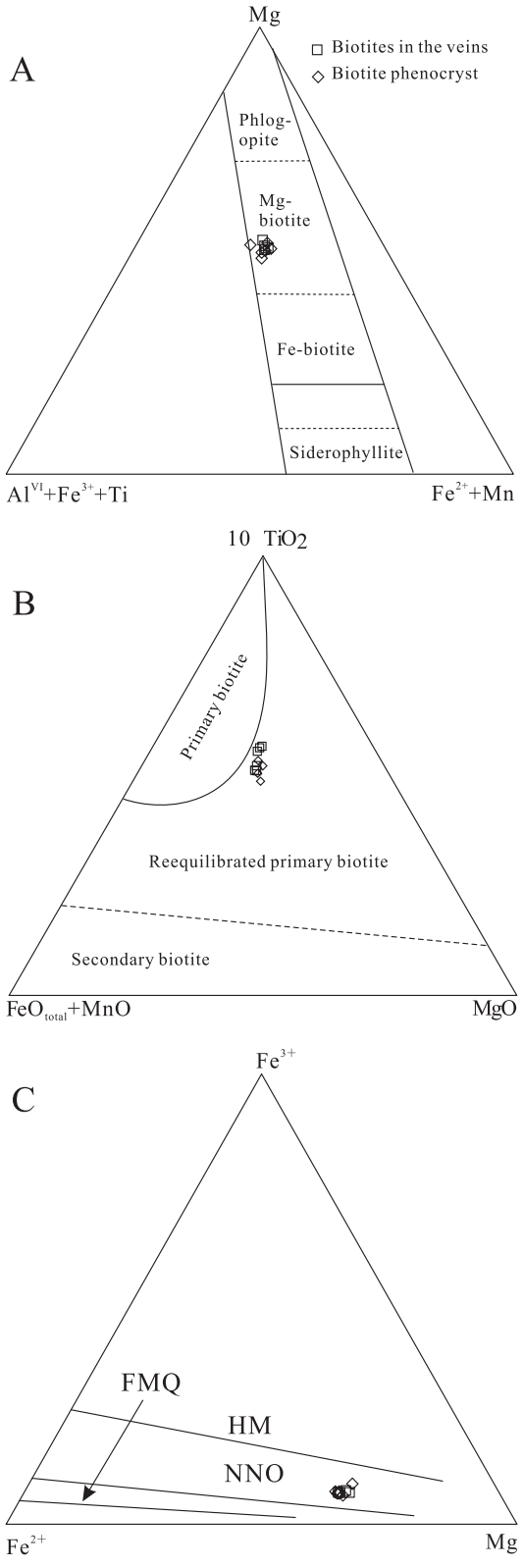


**Fig. 6** Biotites from the potassic alteration zone are plotted in the Mg-rich biotites field of Mg–($Al^{VI}+Fe^{3+}+Ti$)–($Fe^{2+}+Mn$) ternary diagram (a) (Foster, 1960), in the re-equilibrated primary biotite field of the 10 × $TiO_2$-$FeO_{total}$-MgO diagram (b) (Nachit *et al.*, 2005), and plotted in the field between the Ni-NiO (NNO) and $Fe_2O_3$-$Fe_3O_4$ (HM) of the $Fe^{3+}$-$Fe^{2+}$-Mg diagram (c) (Wones & Eugster, 1965).

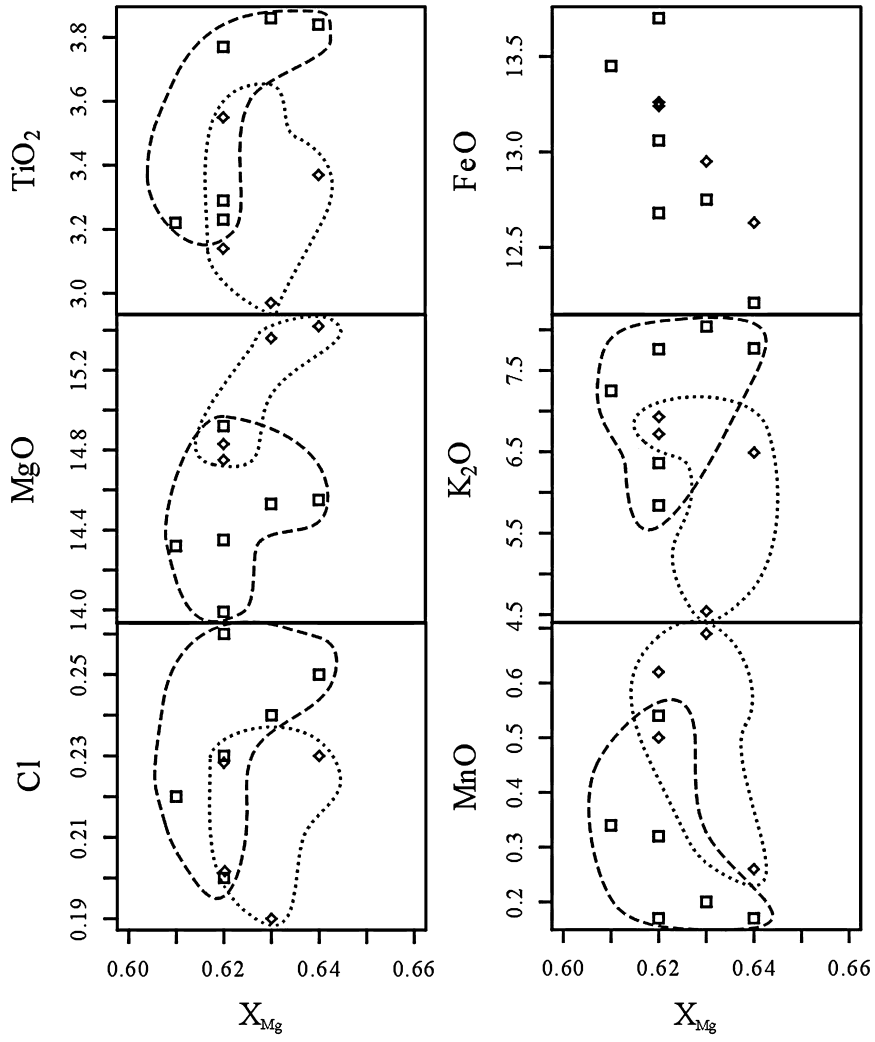


**Fig. 7** $X_{Mg}$ versus the compositions of biotites from the potassic zone, showing the biotite phenocrysts have slightly higher $TiO_2$, MgO, $K_2O$, Cl and MnO content than the veinlet biotites, and the FeO content is negatively correlated with the $X_{Mg}$ of these biotites.

$$CuCl_2 + H_2O + FeS_2 = CuFeS_2 + 2H^+ + 1/2O_2 + 2Cl.$$

Overall, as the temperature decreased, the oxygen fugacity ($fO_2$) of magma and ore-forming fluid first decreases from the magma stage and the potassic alteration stage to the argillic stage, and then gradually increases (Fig. 13b).

## 5.2 Variations of F, Cl, $SO_3$ and other mineral compositions and their significance

### *5.2.1 Biotite halogen chemistry*

Biotite with high $X_{Mg}$ values incorporates less Cl than that with lower $X_{Mg}$ values, an effect referred to as the Mg-Cl avoidance principle (Munoz, 1984). The Cl content of biotite in the potassic zone appears to be independent of the $X_{Mg}$ content, suggesting either that the Mg:Cl crystal-chemical effect does not apply to these biotites or low and high $X_{Mg}$-bearing biotite coexisted with locally Cl-rich and Cl-poor hydrothermal fluid.

Biotite from the potassic zone at the Duolong deposit possesses log ($X_{Cl}/X_{OH}$) values ranging from –2.74 to –2.88 (Fig. 14, Table 3). Zhu and Sverjensky (1992) identified that the composition of biotite formed under similar physicochemical conditions produces linear trends on log ($X_{Cl}/X_{OH}$) versus $X_{Fe}$ and log ($X_{Cl}/X_{OH}$) versus $X_{Mg}$ plots. The slopes of

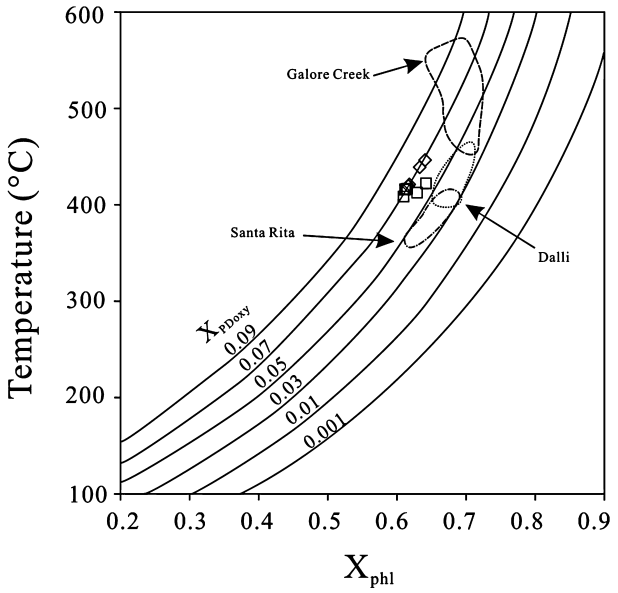


**Fig. 8** Compositions of biotite from the potassic alteration zone at Duolong deposit on Beane's (1974) $X_{phl}$ versus temperature (°C) diagram. Contours show the fixed mole fractions of proton-deficient oxyannite. Analytical data for the plotting of other porphyry copper deposits including Galore Creek and Santa Rita are taken from Beane (1974). Biotite compositions from Dalli porphyry copper deposit are taken from Ayati *et al*. (2008).

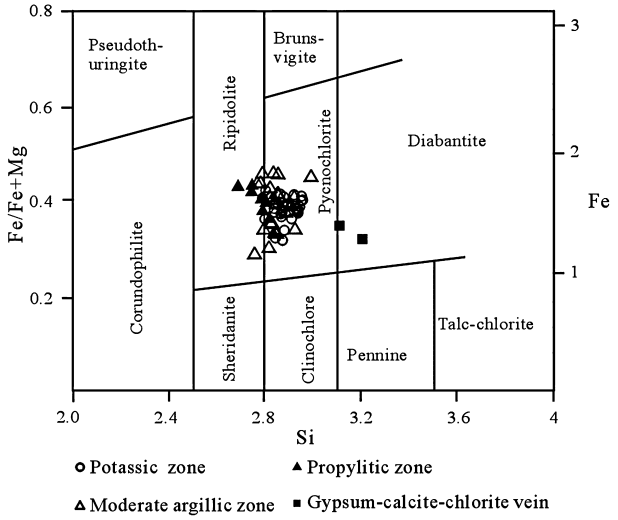


**Fig. 9** The classification of chlorites from the Duolong deposit (after Hey, 1954).

these trends are a function of temperature, and independent of pressure and fluid composition, whereas the y-intercept value is a function of all these parameters (Zhu & Sverjensky, 1992). Using the median formation temperature (T = 420°C) of biotite established by biotite geothermometer (Beane, 1974), the slopes for the log ($X_{Cl}/X_{OH}$) versus $X_{Fe}$ and log ($X_{Cl}/X_{OH}$) versus $X_{Mg}$ plots are derived from Eqs. 23 and 24 of Zhu and Sverjensky (1992). These calculated slopes are –1.6 and –0.72, respectively. In the log ($X_{Cl}/X_{OH}$) versus $X_{Fe}$ and log ($X_{Cl}/X_{OH}$) versus $X_{Mg}$ plots (Fig. 14), the Cl content of biotite from the potassic zone defines linear trends without a broad scatter. The y-intercepts in these plots for biotite from the potassic zone are –2.1 and –2.4, respectively (Fig. 14). Therefore, the similar intercept values and the narrow scatter for the log ($X_{Cl}/X_{OH}$) ratios may suggest that hydrothermal fluids were nearly constant during the potassic alteration, forming under relatively similar temperature conditions.

The chlorine intercept [IV (Cl)] value is an important physicochemical parameter to describe the Cl content in mica, which was defined by Munoz (1984). Biotite have IV (Cl) values of –3.48 to –3.35 (mean = –3.41). The range at Duolong is consistent with the range of intercept values of IV (Cl) (–5.0 to –2.7) biotites from other worldwide porphyry copper deposits (Munoz, 1984; Loferski & Ayuso, 1995; Selby & Nesbitt, 2000; Yavuz, 2003). Chlorine data in biotite was used to estimate the log ($fH_2O/fHCl$) ratio for hydrothermal fluids, which are responsible for the mineralization and hydrothermal alteration processes at the Duolong deposit. The fugacity ratio was estimated by using the equations proposed by Munoz (1992), which are based on the revised coefficients for F–Cl–OH partitioning between biotite and hydrothermal fluid (Zhu & Sverjensky, 1991, 1992). Biotites from the potassic alteration zone have the ($fH_2O/fHCl$) value of 5.55 to 5.70 (mean = 5.62).

Compared with the fugacity ratios of other porphyry copper deposits such as Bingham (Lanier *et al*., 1978; Parry *et al*., 1978; Bowman *et al*., 1987), Casino (Selby & Nesbitt, 2000), Dalli (Ayati *et al*., 2008), Miduk (Boomeri *et al*., 2009) and Batu Hijau (Idrus *et al*., 2007), hydrothermal fluids associated with the potassic alteration at Duolong possess higher log ($fH_2O/fCl$) and IV (Cl) values than these deposits (Fig. 15). The higher activity of chlorine (rather than fluorine) may indicate the significant role of chloride complexes ($CuCl_2^-$ and $AuCl_2^-$) in transporting and precipitating copper and gold at the Duolong deposit.

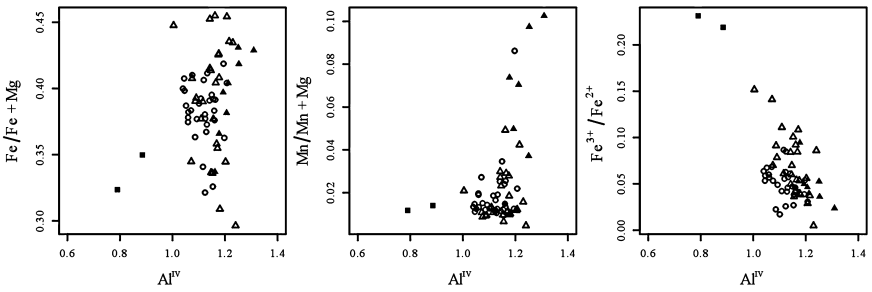


**Fig. 10** The Fe/Fe+Mg, Mn/Mn+Mg and $Fe^{3+}/Fe^{2+}$ ratio versus $Al^{IV}$ of chlorites from the Duolong deposit.

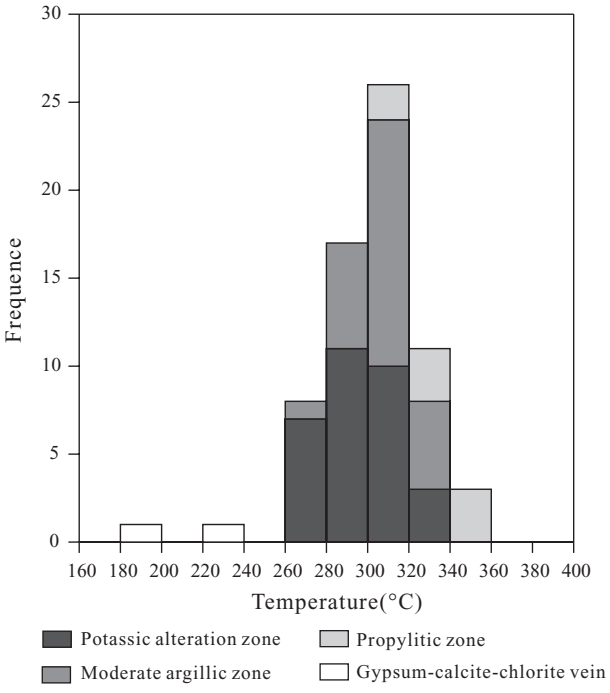


**Fig. 11** Comparison of temperatures of chlorites from the Duolong deposit, Chlorite geothermometry was used according to Cathelineau (1988) and Jowett (1991).

### *5.2.2 Halogen chemistry and $SO_3$ content in apatite*

Apatite inclusions in the biotite phenocrysts have high Cl content (1–1.37%), which is consistent with magmatic apatites from many porphyry copper deposits around the world (Imai, 2000, 2004; Suerte *et al*., 2009). High-temperature, high-salinity fluid inclusions (homogenization temperatures ranging from 620°C to 960°C; salinity ranging from 34 to 82 wt.% NaCl equivalent) have been observed in quartz phenocrysts of the granodiorite porphyry. The primary fluids may have directly exsolved from magma at depths of approximately 7 km (Li *et al*., 2007; Li *et al*., 2011b). High salinity primary fluid indicates the magma has a high Cl/OH ratio, which permits the formation of Cl-rich apatite. Therefore, magmatic apatite inclusions in the biotite phenocrysts showing high $SO_3$ content (0.44–0.82%) and high Cl content (1–1.37%) indicate the high oxidation state (Peng *et al*., 1997) and S and Cl contents of ore-forming magma, which contribute to the formation of porphyry copper deposits (Streck & Dilles, 1998; Imai, 2004).

Apatites from the potassic zone have lower Cl content (0.96–1.44%) than those from the propylitic zone (Cl content of 1.04–2.29%), and are higher than those from the argillic zone (Cl content of 0–1.05%). According to Korzhinskiy (1981) the three solid-solution endmembers of apatite (Cl, F and OH) can be used as indicators of the composition of hydrothermal fluids. He also showed that the Cl/F ratio in apatite increases with temperature and that the pressure effects on the distribution for the components are negligible at 500–700°C. Zhu and Sverjensky (1991) demonstrated that partitioning of F and Cl between minerals and hydrothermal fluids is a strong function of temperature, pressure, pH and fluid composition. Increase of temperature favors partitioning of F into fluids, while it favors partitioning of Cl into minerals. The decrease of both pressure and pH of fluids favors partitioning of Cl into minerals (Zhu & Sverjensky, 1991). At Duolong, the propylitic zone formed by the fluid of lower Cl content and higher pH under a lower temperature (Li *et al*., 2007), suggesting Cl of fluid into apatite should be hindered (Korzhinskiy, 1981; Zhu & Sverjensky, 1991). Therefore, the highest Cl content of apatites from the propylitic zone may have resulted from the decrease of pressure, whereas, the lowest Cl content of apatites from the moderate argillic zone may be caused by the low Cl content of fluids. In contrast,

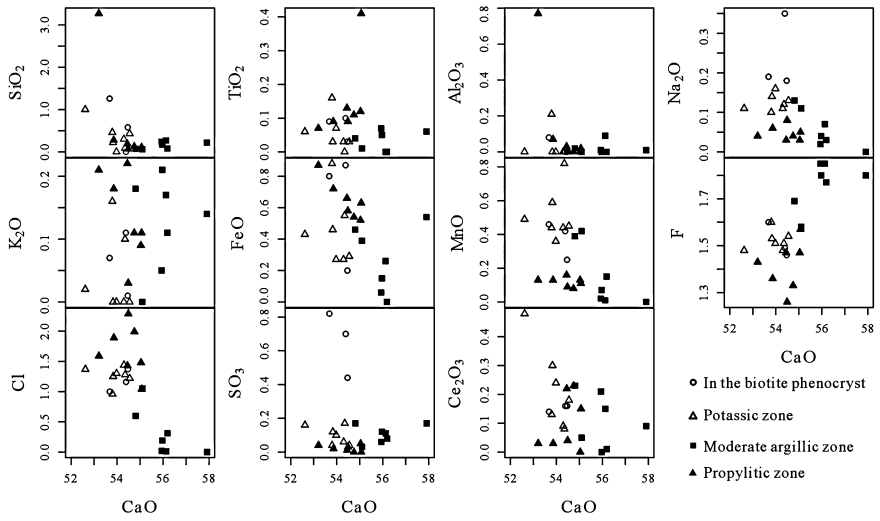


**Fig. 12** Compositions of apatites versus CaO content at the Duolong deposit.

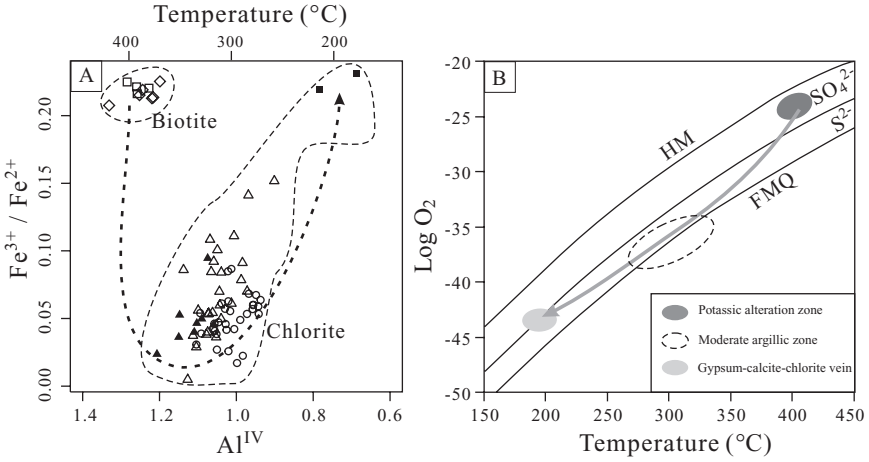


**Fig. 13** The diagram (a) of $Fe^{3+}/Fe^{2+}$ ratio versus $Al^{IV}$ of biotites and chlorites, and the diagram (b) of oxygen fugacity ($fO_2$) versus temperature (t). These show that changing oxygen fugacity of fluids during the process of decreasing temperature and magmatic–hydrothermal evolution. Hematite-magnetite (HM) and fayalite-magnetite-quartz (FMQ) buffer curve for oxygen fugacity are calculated by the equation of Schwab and Kustner (1981) and O'Neill (1987). The boundary between $SO_4^{2-}$ and $S^{2-}$ is calculated by the equation of Carroll and Rutherford (1988).

F content of apatite shows opposite variation trends, possibly controlled by the decrease of temperature.

The $SO_3$ content decreases from apatite inclusions in the biotite phenocrysts, the potassic zone, the argillic zone and to the propylitic zone. The $SO_3$ contents of apatite increase with increasing oxygen fugacity (Peng *et al*., 1997) and $SO_3$ content of magma and fluid. Sulfate sulfur into the apatite crystal structure predominantly is by the coupled exchange reaction of $S^{6+} + Si^{4+} = 2P^{5+}$ (Rouse & Dunn, 1982) and $S^{6+} + Na^{+} = P^{5+} + Ca^{2+}$ (Liu & Comodi, 1993). Therefore, the decreasing $SO_3$ content may have resulted from the reducing oxygen fugacity and $SO_3$ content of fluid. This is also evidenced from formation of abundant magnetite, minor rutile and sulfides in the potassic zone, because the precipitation of magnetite decreases the oxygen fugacity and $SO_3$ content of fluid (Sun *et al*., 2004; Li *et al*., 2006; Liang *et al*., 2009):

$$12\,(FeO) + H_2SO_4 = 4\,Fe_3O_4 + H_2S.$$

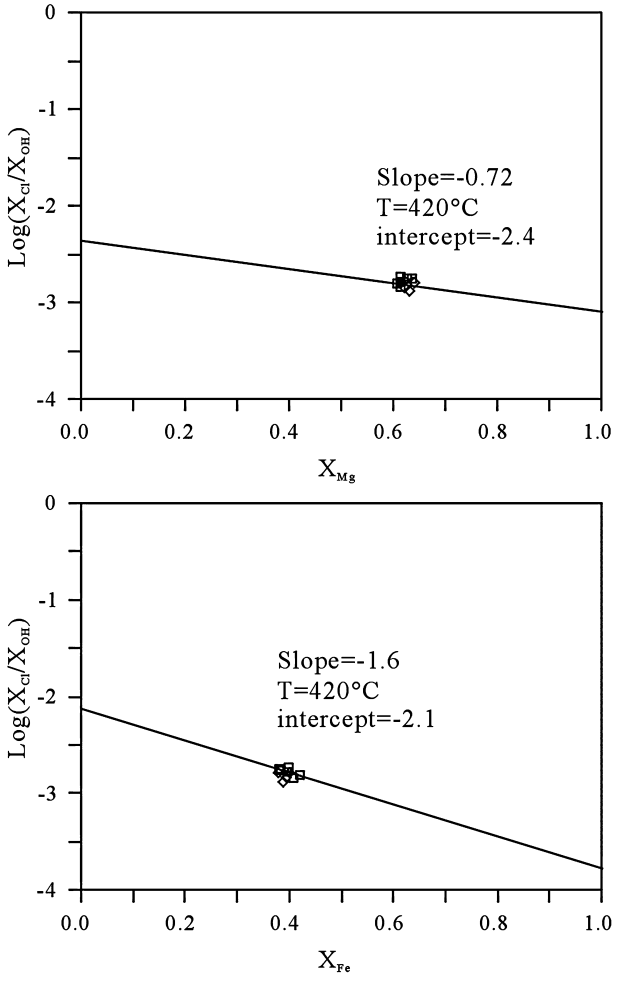


**Fig. 14** Log ($X_{Cl}/X_{OH}$) versus $X_{Mg}$ and $X_{Fe}$ of biotites from the potassic zone at the Duolong deposit.

$$12\ FeCl_2 + 12\ H_2O + H_2SO_4 = 4\ Fe_3O_4 + 24\ HCl + H_2S$$

These observations are consistent with FeO content of apatite decreasing from the potassic to the argillic zone, whereas, the higher FeO content of apatites from the propylitic zone may be caused by the composition (high FeO content) of basaltic wall rock. In addition, $Na_2O$ content of apatites decreases from the inclusions in biotite phenocrysts, the potassic zone, and to the propylitic zone, possibly confirming the substitution mechanism of $S^{6+} + Na^{+} = P^{5+} + Ca^{2+}$ (Liu & Comodi, 1993). However, apatite with the lowest $Na_2O$ content has no lowest $SO_3$ content in the argillic zone, which is not consistent with this substitution. The observation possibly implies the ore-forming fluid was relatively deficient in Na, in accordance with the result of a fluid inclusion study for the argillic zone (Li *et al*., 2007). Therefore, the $Na_2O$ content of apatite may be controlled both by this substitution mechanism and the Na content of ore-forming fluid.

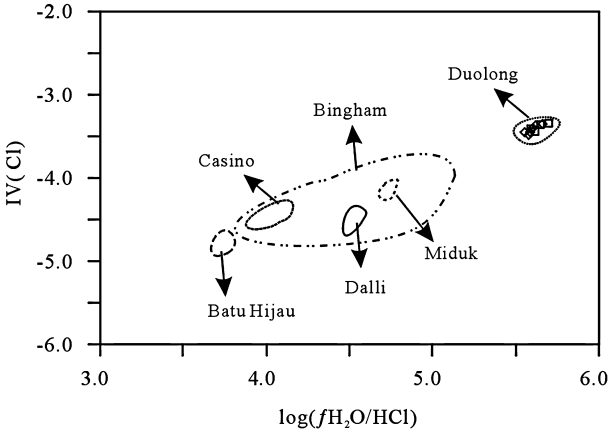


**Fig. 15** Comparsion of the Duolong deposit with other porphyry deposits in terms of Log ($X_{Cl}/X_{OH}$) versus IV (Cl) of biotites; analytical data for the plotting of other porphyry copper deposits including Bingham (Lanier *et al*., 1978; Parry *et al*., 1978; Bowman *et al*., 1987), Casino (Selby & Nesbitt, 2000), Dalli (Ayati *et al*., 2008), Miduk (Boomeri *et al*., 2009) and Batu Hijau (Idrus *et al*., 2007).

## 6. Conclusions

The Duolong gold-rich porphyry copper deposit contains abundant magnetite associated with Cu-Au mineralization. During the mineralization and hydrothermal alteration, various hydrothermal minerals formed, and these minerals can help us to understand the magmatic-hydrothermal process. Through the detailed microscropic observation and EMPA analysis of these minerals, the following conclusions are obtained.

**1** Secondary K-feldspar replaces mainly plagioclase phenocryst and occurs as veinlets. The K-feldspar shows high contents of Or (75.1–96.9%) with minor amounts of Ab (3.0–24.4%) and negligible An (0–0.6%). Secondary albite replaces mainly plagioclase phenocryst along its rim and fissures. The albite shows high contents of Ab (91.5–99.7%) with negligible amounts of An (0.2–8.2%) and Or (0.1–1.1%).

**2** Biotite from the potassic zone occurs as veinlets and dissemination. All the biotites belong to the Mg-rich

biotites ($X_{Mg}$ = 0.61–0.64), and formed under high oxidation conditions and temperatures ranging from 400°C to 430°C. Biotite phenocrysts are re-equilibrated with late-stage hydrothermal fluids in the potassic zone. Re-equilibrated biotite phenocrysts show slightly higher $TiO_2$, MgO, $K_2O$, Cl and MnO contents than the veinlet biotites, indicating they inherit the characters of primary magmatic biotite. All the biotites are absent of F, and have high Cl content (0.19–0.26%), log ($X_{Cl}/X_{OH}$) values (–2.74 to –2.88), and IV (Cl) values (–3.48 to –3.35). The higher activity of chlorine (rather than fluorine) may indicate the significant role of chloride complexes ($CuCl_2^-$ and $AuCl_2^-$) in transporting and precipitating copper and gold at the Duolong deposit. In the log ($X_{Cl}/X_{OH}$) versus $X_{Fe}$ and log ($X_{Cl}/X_{OH}$) versus $X_{Mg}$ plots, the Cl content of biotite from the potassic zone defines linear trends without a broad scatter, suggesting that the hydrothermal fluid was nearly constant during the potassic alteration, forming under relatively similar temperature conditions.

**3** Secondary chlorites are extensively distributed in all alteration zones, replace biotite and hornblende, and also occur in the chlorite-bearing veinlets. They correspond mainly to pycnochlorite. Chlorites have similar Fe/(Fe+Mg) ratios and Mn/(Mn+Mg). The consistent formation temperature (280–360°C) suggests that chlorite formed at the same temperature in all alteration zones. The formation temperature range of chlorite from the gypsum-carbonate-chlorite vein is between 190°C and 220°C, indicating it may have resulted from the later stage of hydrothermal activity. The $Fe^{3+}/Fe^{2+}$ ratios of chlorites are negatively correlated with $Al^{IV}$. As the temperature decreased, the oxygen fugacity ($fO_2$) of magma and ore-forming fluid first decreased from the magma stage and the early potassic stage to the moderate argillic stage, and then gradually increased.

**4** Magmatic apatite inclusions in the biotite phenocrysts show high $SO_3$ content (0.44–0.82%) and high Cl content (1–1.37%), indicating the ore-forming magma possesses a high oxidation state, both S-rich and Cl-rich. The highest Cl content of apatite from the propylitic zone may have resulted from the decrease of pressure, whereas, the lowest Cl content of apatite from the moderate argillic zone may be caused by the low Cl content of fluids. In addition, the decreasing $SO_3$ content of apatite may have resulted from the reducing oxygen fugacity and $SO_3$ content of fluid, which is caused by the precipitation of abundant magnetite.

## Acknowledgments

This article was funded by NSFC (Natural Science Foundation of China) (40902027, 40672068), the important research direction project of the Academy of Sciences of China (KZCX2-YW-Q04-2) and China Geological Survey project (20089932). We have obtained great support and help from senior geologist Mr. Tianping Zhang and other geologists of the No.5 Geological Team, Tibet Bureau of Geology and Exploration; and obtained specific guidance and assistance from senior engineer Qian Mao, and Yuguang Ma with the EMPA analysis process in the Institute of Geology and Geophysics, Chinese Academy of Sciences.

## References

Ayati, F., Yavuz, F., Noghreyan, M., Haroni, H. A. and Yavuz, R. (2008) Chemical characteristics and composition of hydrothermal biotite from the Dalli porphyry copper prospect, Arak, central province of Iran. Miner. Petrol., 94, 107–122.

Beane, R. E. (1974) Biotite stability in porphyry copper environment. Econ. Geol., 69, 241–256.

Boomeri, M., Nakashima, K. and Lentz, D. R. (2009) The Miduk porphyry Cu deposit, Kerman, Iran: A geochemical analysis of the potassic zone including halogen element systematics related to Cu mineralization processes. J. Geochem. Explor., 103, 17–29.

Bowman, J. R., Parry, W. T., Kropp, W. P. and Kruer, S. A. (1987) Chemical and Isotopic Evolution of Hydrothermal Solutions at Bingham, Utah. Econ. Geol., 82, 395–428.

Carroll, M. R. and Rutherford, M. J. (1988) Sulfur speciation in hydrous experimental glasses of varying oxidation-state—Results from measured wavelength shifts of sulfur X-Rays. Am. Mineral., 73, 845–849.

Cathelineau, M. (1988) Cation Site occupancy in chlorites and illites as a function of temperature. Clay Mineral., 23, 471–485.

Dymek, R. F. (1983) Titanium, aluminum and interlayer cation substitutions in biotite from high-grade gneisses, West Greenland. Am. Mineral., 68, 880–899.

Foster, M. D. (1960) Interpretation of the composition of trioctahedral micas. US. Geol. Surv., Prof. Pap., 354-B, 1–146.

Gustafson, L. B. and Hunt, J. P. (1975) The porphyry copper deposit at El Salvador, Chile. Econ. Geol., 70, 857–912.

Gustafson, L. B. and Quiroga, G. J. (1995) Patterns of mineralization and alteration below the porphyry copper orebody at El Salvador, Chile. Econ. Geol., 90, 2–16.

Hey, M. H. (1954) A new review of the chlorites. Mineral. Mag., 30, 277–292.

Hou, Z. Q., Gao, Y. F., Qu, X. M., Rui, Z. Y. and Mo, X. X. (2004) Origin of adakitic intrusives generated during mid-Miocene East-west extension in southern Tibet. Earth Planet. Sci. Let., 220, 139–155.

Hou, Z. Q., Ma, H. W., Zaw, K., Zhang, Y. Q., Wang, M. J., Wang, Z., Pan, G. T. and Tang, R. L. (2003) The Himalayan Yulong porphyry copper belt: Product of large-scale strike-slip faulting in eastern Tibet. Econ. Geol., 98, 125–145.

Hou, Z. Q., Yang, Z. M., Qu, X. M., Meng, X. J., Li, Z. Q., Beaudoin, G., Rui, Z. Y., Gao, Y. F. and Zaw, K. (2009) The Miocene Gangdese porphyry copper belt generated during post-collisional extension in the Tibetan Orogen. Ore Geol. Rev., 36, 25–51.

Hou, Z. Q., Zaw, K., Pan, G. T., Mo, X. X., Xu, Q., Hu, Y. Z. and Li, X. Z. (2007) Sanjiang Tethyan metallogenesis in SW China: Tectonic setting, metallogenic epochs and deposit types. Ore Geol. Rev., 31, 48–87.

Idrus, A., Kolb, J. and Meyer, E. M. (2007) Chemical composition of rock-forming minerals in copper-gold-bearing tonalite porphyries at the Batu Hijau deposit, Sumbawa Island, Indonesia: Implications for crystallization conditions and fluorine-chlorine fugacity. Resour. Geol., 57, 102–113.

Imai, A. (2000) Genesis of the Mamut porphyry copper deposit, Sabah, East Malaysia. Resour. Geol., 50, 1–23.

Imai, A. (2004) Variation of Cl and $SO_3$ contents of microphenocrystic apatite in intermediate to silicic igneous rocks of Cenozoic Japanese island arcs: Implications for porphyry Cu metallogenesis in the Western Pacific Island arcs. Resour. Geol., 54, 357–372.

Jowett, E. C. (1991) Fitting iron and magnesium into the hydrothermal chlorite geothermometer. GAC/MAC/SEG Joint Annual Meeting (Tront) Abstract, A62.

Korzhinskiy, M. A. (1981) Apatite solid solutions as indicators of the fugacity of HCl and HF in hydrothermal fluids. Geochem. Int., 3, 45–60.

Lanier, G., Raab, W. J., Folsom, R. B. and Cone, S. (1978) Alteration of equigranular monzonite, Bingham mining district, Utah. Econ. Geol., 73, 1270–1286.

Li, G. M., Li, J. X., Qin, K. Z., Duo, J., Zhang, T. P., Xiao, B. and Zhao, J. X. (2012) Geology and hydrothermal alteration of the Duobuza gold-rich porphyry copper district in the Bangongco metallogenetic belt, Northwestern Tibet. Resour. Geol., 62, 98–118.

Li, G. M., Li, J. X., Qin, K. Z., Zhang, T. P. and Xiao, B. (2007) High temperature, salinity and strong oxidation ore-forming fluid at Duobuza gold-rich porphyry copper in the Bangonghu tectonic belt, Tibet: Evidence from fluid inclusions study. Acta Petrol. Sinica, 23, 935–952 (in Chinese with English abstr.).

Li, J. X., Li, G. M., Qin, K. Z. and Xiao, B. (2008) Geochemistry of porphyries and volcanic rocks and ore-forming geochronology of Duobuza gold-rich porphyry copper deposit in Bangonghu belt, Tibet: Constraints on metallogenetic tectonic settings. Acta Petrol. Sinica, 24, 531–543 (in Chinese with English abstr.).

Li, J. X., Li, G. M., Qin, K. Z. and Xiao, B. (2011b) High temperature magmatic fluid exsolved from magma at Duobuza porphyry copper-gold deposit, Northern Tibet. Geofluids, 11, 134–143.

Li, J. X., Li, G. M., Qin, K. Z., Xiao, B., Zhao, J. X. and Chen, L. (2011a) Magmatic-hydrothermal evolution of the Cretaceous Duolong gold-rich porphyry copper deposit in the Bangongco metallogenetic belt, Tibet: evidence from U-Pb and $^{40}Ar/^{39}Ar$ geochronology. J. Asian Earth Sci., 41, 525–536.

Li, J. X., Qin, K. Z. and Li, G. M. (2006) The basic characteristics of gold–rich porphyry copper deposits and their ore sources and evolving processes of high oxidation magma and ore-forming fluid. Acta Petrologica Sinica, 22, 678–688 (in Chinese with English abstr.).

Liang, H. Y., Sun, W. D., Su, W. C. and Zartman, R. E. (2009) Porphyry Copper-gold mineralization at Yulong, China, promoted by decreasing redox potential during magnetite alteration. Econ. Geol., 104, 587–596.

Liu, Y. and Comodi, P. (1993) Some aspects of the crystal-chemistry of apatites. Mineral. Mag., 57, 709–719.

Loferski, P. J. and Ayuso, R. A. (1995) Petrography and mineral chemistry of the composite Deboullie pluton, Northern Maine, USA—Implications for the genesis of Cu-Mo mineralization. Chem. Geol., 123, 89–105.

Munoz, J. L. (1984) F-OH and Cl-OH exchange in micas with applications to hydrothermal ore-deposits. In Bailey, S.W. (ed.), Rev. Mineral., 13, 469–493.

Munoz, J. L. (1992) Calculation of HF and HCl fugacities from biotite compositions: revised equations. Geol. Soc. Am., Abstract Programs 24, A221.

Nachit, H., Ibhi, A., Abia, E. H. and Ohoud, M. B. (2005) Discrimination between primary magmatic biotites, reequilibrated biotites and neoformed biotites. C. R. Geosci., 337, 1415–1420.

O'Neill, H. S. (1987) Quartz-fayalite-iron and quartz-fayalite-magnetite equilibria and the free-energy of formation of fayalite ($Fe_2SiO_4$) and magnetite ($Fe_3O_4$). Am. Mineral., 72, 67–75.

Parat, F., Dungan, M. A. and Streck, M. J. (2002) Anhydrite, pyrrhotite, and sulfur-rich apatite: tracing the sulfur evolution of an Oligocene andesite (Eagle Mountain, CO, USA). Lithos, 64, 63–75.

Parry, W. T., Ballantyne, G. H. and Wilson, J. C. (1978) Chemistry of biotite and apatite from a vesicular quartz latite porphyry plug at Bingham, Utah. Econ. Geol., 73, 1308–1314.

Peng, G. Y., Luhr, J. F. and McGee, J. J. (1997) Factors controlling sulfur concentrations in volcanic apatite. Am. Mineral., 82, 1210–1224.

Qin, K. Z., Li, G. M., Zhang, Q., Li, J. X., Maio, Y., Xiao, B., Zhang, T. P., Duo, J., Li, J. G. and Lu, Y. (2006) Metallogenic conditions and possible occurrences for epithermal gold mineralizations in Gangdese and Bangonghu Belts, Tibet—In view of porphyry-epithermal Cu-Au metallogenetic systematics. Proceedings of 8th State Mineral Deposit Conference, Geological Publishing House, Beijing: 660–670 (in Chinese).

Qin, K. Z., Li, G. M., Zhao, J. X., Li, J. X., Xue, G. Q., Yan, G., Su, D. K., Xiao, B., Chen, L. and Fan, X. (2008) Discovery of Sharang large-scale porphyry molybdenum deposit, the first Single Mo deposit in Tibet and its significance. Geol.. China, 35, 1101–1112 (in Chinese with English abstr.).

Qin, K. Z., Tosdal, R. M., Li, G. M., Zhang, Q. and Li, J. L. (2005) Formation of the Miocene porphyry Cu (-Mo-Au) deposits in the Gangdese arc, southern Tibet, in a transitional tectonic setting. Mineral Deposit. Res. Meet. Chall., 3, 44–47.

Rouse, R. C. and Dunn, P. J. (1982) A contribution to the crystal chemistry of ellestadite and the silicate sulfate apatites. Am. Mineral., 67, 90–96.

Schwab, R. G. and Kustner, D. (1981) The equilibrium fugacities of important oxygen buffers in technology and petrology. Neues Jahr. Fur Mineral., 140, 112–142.

Scott, K. M. (2005) Rutile geochemistry as a guide to porphyry Cu-Au mineralization, Northparkes, New South Wales, Australia. Geochem. Explor. Env. A, 5, 247–253.

Selby, D. and Nesbitt, B. E. (2000) Chemical composition of biotite from the Casino porphyry Cu-Au-Mo mineralization, Yukon, Canada: evaluation of magmatic and hydrothermal fluid chemistry. Chem. Geol., 171, 77–93.

Streck, M. J. and Dilles, J. H. (1998) Sulfur evolution of oxidized arc magmas as recorded in apatite from a porphyry copper batholith. Geology, 26, 523–526.

Suerte, L. O., Imai, A. and Nishihara, S. (2009) Geochemical Characteristics of Intrusive Rocks, Southeastern Mindanao, Philippines: Implication to Metallogenesis of Porphyry Copper-gold Deposits. Resour. Geol., 59, 244–262.

Sun, W. D., Arculus, R. J., Kamenetsky, V. S. and Binns, R. A. (2004) Release of gold-bearing fluids in convergent margin magmas prompted by magnetite crystallization. Nature, 431, 975–978.

Wones, D. R. and Eugster, H. P. (1965) Stability of biotite—experiment theory and application. Am. Mineral., 50, 1228–1272.

Yavuz, F. (2003) Evaluating micas in petrologic and metallogenic aspect: Part II-applications using the computer program Mica (+). Comput. Geosci., 29, 1215–1228.

Zhu, C. and Sverjensky, D. A. (1991) Partitioning of F-Cl-OH between minerals and hydrothermal fluids. Geochim. Cosmochim. Acta, 55, 1837–1858.

Zhu, C. and Sverjensky, D. A. (1992) F-Cl-OH partitioning between biotite and apatite. Geochim. Cosmochim. Acta, 56, 3435–3467.